

1 **Biological Production in the Indian Ocean Upwelling Zones, Part – I: Refined Estimation**
2 **via the Use of a Variable Compensation Depth in Ocean Carbon Models**

3

4 Mohanan Geethalekshmi Sreeush^{1,2,*}.

5 Vinu Valsala¹,

6 Sreenivas Pentakota¹,

7 Koneru Venkata Siva Rama Prasad²,

8 Raghu Murtugudde³

9

10 ¹Indian Institute of Tropical Meteorology, Pune, India

11 ²Department of Meteorology and Oceanography, Andhra University, India

12 ³ESSIC, University of Maryland, USA

13

14 *(Under revision BGD)*

15

16 *Corresponding author address:

17 Indian Institute of Tropical Meteorology,

18 Dr. Homi Bhabha Road, Pashan, Pune 411 008, India

19 E-Mail: sreeushmg@tropmet.res.in

20

21 **Abstract**

22

23 Biological modeling approach adopted by the Ocean Carbon-cycle Model Inter-comparison
24 Project (OCMIP-II) provided amazingly simple but surprisingly accurate rendition of the annual
25 mean carbon cycle for the global ocean. Nonetheless, OCMIP models are known to have
26 seasonal biases which are typically attributed to their bulk parameterization of ‘compensation
27 depth’. Utilizing the criteria of surface Chl-a based attenuation of solar radiation and the
28 minimum solar radiation required for production, we have proposed a new parameterization for a
29 spatially and temporally varying ‘compensation depth’ which captures the seasonality in the
30 production zone reasonably well. This new parameterization is shown to improve the seasonality
31 of CO₂ fluxes, surface ocean pCO₂, biological export and new production in the major upwelling
32 zones of the Indian Ocean. The seasonally varying compensation depth enriches the nutrient
33 concentration in the upper ocean yielding more faithful biological exports which in turn leads to
34 an accurate seasonality in the carbon cycle. The export production strengthens by ~70% over the
35 western Arabian Sea during monsoon period and achieves a good balance between export and
36 new production in the model. This underscores the importance of having a seasonal balance in
37 model export and new productions for a better representation of the seasonality of carbon cycle
38 over upwelling regions. The study also implies that both the biological and solubility pumps play
39 an important role in the Indian Ocean upwelling zones.

40

41 Keywords: Indian Ocean upwelling zones, Carbon cycle, Seasonal cycle - CO₂ flux and Oceanic
42 pCO₂, Biogeochemical model parameterization, Export production - New production balance,
43 Solubility and Biological pump.

44

45 **1. Introduction**

46 The Indian Ocean is characterized by the unique seasonally reversing monsoon wind systems
47 which act as the major physical drivers for the coastal and open ocean upwelling processes. The
48 major upwelling systems in the Indian Ocean are (1) the western Arabian Sea (WAS; Ryther and
49 Menzel, 1965; Smith et al., 2001; Sarma, 2004; Wiggert et al., 2005, 2006; Murtugudde et al.,
50 2007; McCreary et al., 2009; Prasanna Kumar et al., 2010; Naqvi et al., 2010; Roxy et al., 2015)
51 (2) the Sri Lanka Dome (SLD; Vinayachandran et al., 1998, 2004), (3) Java and Sumatra coasts
52 (SC; Murtugudde et al., 1999a; Susanto et al., 2001; Osawa et al., 2010; Xing et al., 2012) and
53 (4) the Seychelles-Chagos thermocline ridge (SCTR; Murtugudde et al., 1999b; Dilmahamod et
54 al., 2016, Figure 1). The physical and biological processes and their variability over these key
55 regions are inseparably tied to the strength of the monsoon winds and associated nutrient
56 dynamics. The production and its variability over these coastal upwelling systems are a key
57 concern for the fishing community, since they affect the day-to-day livelihood of the coastal
58 populations (Harvell et al., 1999; Roxy et al., 2015; Praveen et al., 2016) and are important for
59 the Indian Ocean rim countries due to their developing country status.

60 Arabian Sea is a highly productive coastal upwelling system characterized by phytoplankton
61 blooms both in summer (Prasanna Kumar et al., 2001; Naqvi et al., 2003; Wiggert et al., 2005)
62 and winter (Banse and McClain, 1986; Wiggert et al., 2000; Barber et al., 2001; Prasannakumar
63 et al., 2001; Sarma, 2004). The Arabian Sea is known for the second largest Tuna fishing region
64 in the Indian Ocean (Lee et al., 2005). The Somali and Omani upwelling regions experience
65 phytoplankton blooms that are prominent with Net Primary Production (NPP) exceeding 435 g C
66 m⁻² yr⁻¹ (Liao et al., 2016). On the other hand productivity over the SLD (Vinayachandran and
67 Yamagata, 1998) is triggered by open ocean Ekman suction with strong Chl-a blooms during the

68 summer monsoon (Murtugudde et al., 1999a; Vinayachandran et al., 2004). Similarly, the SC
69 upwelling is basically due to the strong alongshore winds and its variation is associated with the
70 impact of equatorial and coastal Kelvin waves (Murtugudde et al., 2000, Valsala and Rao, 2016).
71 The interannual variability associated with the Java-Sumatra coastal upwelling is strongly
72 coupled with ENSO (ElNiño Southern Oscillation) through the Walker cell and Indonesian
73 throughflow (Susanto et al., 2001; Valsala et al., 2011) and peaks in July through August with a
74 potential new production of 0.1 Pg C yr^{-1} (Xing et al., 2012). The SCTR productivity has a large
75 spatial and interannual variability. The warmer upper ocean condition associated with El Niño
76 reduces the amplitude of subseasonal SST variability over the SCTR (Jung and Kirtman., 2016).
77 The Chl-a concentration peaks in summer when the southeast trade winds induce mixing and
78 initiate the upwelling of nutrient-rich water (Murtugudde et al., 1999a; Wiggert et al., 2006;
79 Vialard et al., 2009; Dilmahamod et al., 2016).

80 Understanding the biological production and variability in the upwelling systems is important
81 because it gives us crucial information regarding marine ecosystem variability (Colwell, 1996;
82 Harvell et al., 1999). The observations also provide vital insights into physical and biological
83 interactions of the ecosystem (Naqvi et al., 2010) as well as the biophysical feedbacks
84 (Murtugudde et al., 1999a), although limitations of sparse observations often force us to depend
85 on models to examine the large spatio-temporal variability of the ecosystem (Valsala et al.,
86 2013). Simple to intermediate complexity marine ecosystem models have been employed by
87 several of the previous studies (Sarmiento et al., 2000; Orr et al., 2001; Matsumoto et al., 2008).
88 However, the representation of marine ecosystem with proper parameterizations in models has
89 always been a daunting task. This is an impediment to the accurate representation of biological

90 primary and export productions in models (Friedrichs et al., 2006, 2007) and these issues also
91 impact the modeling of upper trophic levels (Lehodey et al., 2010).

92 Biological production can be quantified with a better understanding of primary production
93 which depends on water temperature, light and nutrient availability (Brock et al., 1993; Moisan
94 et al., 2002) and this became the key reason for parameterizing the production in models as one
95 or more combinations of these terms (Yamanaka et al., 2004). Any of these basic parameters can
96 be tweaked to alter production in models. For example, the availability of nutrients and light
97 determines the phytoplankton growth (Eppely et al., 1972) or growth rate (Boyd et al., 2013).
98 Stoichiometry and carbon-to-Chl-a ratios are other important factors to be considered in
99 modeling (Christian et al., 2001, Wang et al., 2009) but we will not consider them in this study.

100 The Ocean Carbon-cycle Model Intercomparison Project (OCMIP) greatly improved our
101 understanding of global carbon cycle (Najjar and Orr, 1998). OCMIP-II further introduced a
102 simple phosphate-dependent production term in biological models for long-term simulations of
103 the carbon cycle in response to anthropogenic climate change with an accurate annual mean state
104 (Najjar and Orr, 1998; Orr et al., 2001; Doney et al., 2004). However, the OCMIP – II model
105 simulations come with a penalty of strong seasonal biases when compared with observations
106 (Orr et al., 2003). In this protocol, the community compensation depth (hereafter Z_c) is defined
107 as the depth at which photosynthesis equals entire community respiration and the irradiance at
108 which this balance achieved is the compensation irradiance (E_{com}). Note that Z_c is clearly
109 different from the conventional euphotic zone depth (Morel, 1988). Within Z_c , the production of
110 organic phosphorous representing the biological production (in the present context the Net
111 Community Production; NCP) is given as $J_{prod} = \frac{1}{\tau}([PO_4] - [PO_4^*])$, where $[PO_4]$ is the model
112 phosphate concentration and $[PO_4^*]$ is observational phosphate concentration. τ is the restoration

113 timescale assumed to be 30 days. Whenever the model phosphate exceeds the observational
114 phosphate, it allows production. At Z_c , the NCP is zero and above Z_c the Net Primary
115 Production (NPP) exceeds the community respiration and the ecosystem will grow (Smetacek
116 and Passow, 1990; Gattuso et al., 2006; Sarmiento and Gruber, 2006; Regaudix-de-Gioux and
117 Duarte, 2010; Marra et al., 2014). However, Z_c was held constant in time and space in OCMIP-II
118 models (Najjar and Orr, 1998; Matsumoto et al., 2008) because the OCMIP-II protocol takes a
119 minimalistic approach to biology and simplifies the model calculations with a very limited set of
120 state variables suitable for long term simulations when implemented in coarse resolution models
121 (Orr et al., 2005). However, in reality Z_c varies in space and time (Najjar and Keeling, 1997) just
122 as the euphotic zone depth does as documented in ship measurements (Qasim, 1977, 1982). The
123 variation in Z_c indicates the seasonality of the production zone itself.

124 Most of the biophysical models prescribe a constant value for Z_c , e.g., a default value of
125 $Z_c = 75$ m in OCMIP –II protocol (Najjar and Orr, 1998) and $Z_c = 100$ m in Minnesota Earth
126 System Model (Matsumoto et al., 2008). Depending on the latitude, Z_c varies between 50m and
127 100m in the real world (Najjar and Keeling, 1997). In our study we have attempted a novel
128 biological parameterization scheme for spatially and temporally varying Z_c in the OCMIP–II
129 framework by representing the production as a function of solar radiation (Parsons et al., 1984)
130 and prescribed Chl-a. In this hypothesis, a spatially and temporally varying Z_c is estimated from
131 the vertical attenuation of insolation by the surface Chl-a. The depth at which the insolation
132 reaches the compensation irradiance (chosen as 10 Wm^{-2}) is taken as Z_c . Phosphorous is the
133 basic currency which limits the production within this varying Z_c . This spatially and temporally
134 varying Z_c represents the seasonality in the production zone which is lacking in the original
135 OCMIP-II protocol.

136 Regions of sustained upwelling like the eastern equatorial Pacific are well understood in
137 terms of the role of upwelling in increasing the surface water $p\text{CO}_2$ to drive an outgassing of CO_2
138 into the atmosphere (Feely et al., 2001; Valsala et al., 2014). The Indian Ocean on the other hand
139 experiences only seasonal upwelling which is relatively weak in the deep tropics but stronger off
140 the coasts of Somalia and Oman and in the SLD (Valsala et al., 2013). The relative importance of
141 the solubility vs. biological pump is not well understood. Our focus here on implementing
142 seasonality in Z_c of OCMIP models nonetheless leads to new insights on the impact of improved
143 biological production on surface water $p\text{CO}_2$ and air-sea CO_2 fluxes. The improvements due to
144 the effect of a variable Z_c over the Indian Ocean and the sensitivity experiments where
145 upwelling is muted strongly imply that the biological pump may play as much of a role as the
146 solubility pump in determining surface $p\text{CO}_2$ and CO_2 fluxes over the Indian Ocean.

147 The paper is organized as follows. Model, Data, and Methods are detailed in Section 2.
148 The spatially inhomogeneous Z_c derived with the new parameterization and its impact on
149 simulated seasonality of biology and carbon cycle are detailed in Section 3. Further a conclusion
150 is provided in Section 4.

151

152 **2. Model, Data, and Methods**

153 **2.1. Model**

154 The study utilizes the Offline Ocean Tracer Transport Model (OTTM; Valsala et al., 2008)
155 coupled with OCMIP biogeochemistry model (Najjar and Orr, 1998). OTTM does not compute
156 currents and stratifications (i.e., temperature and salinity) on its own. It is capable of accepting
157 any ocean model or data-assimilated product as physical drivers. The physical drivers prescribed

158 include 4-dimensional currents (u,v), temperature, salinity, and 3-dimensional mixed layer depth,
 159 surface freshwater and heat fluxes, surface wind stress and sea surface height. The resolution of
 160 the model setup is similar to the parent model from which it borrows the physical drivers. With
 161 the given input of Geophysical Fluid Dynamics Laboratory (GFDL) reanalysis data (Chang et.
 162 al., 2012), the zonal and meridional resolutions are 1° with 360 grid points longitudinally and 1°
 163 at higher latitudes but having a finer resolution of 0.8° in the tropics, with 200 latitudinal grid
 164 points. The model has 50 vertical levels with 10m increment in the upper 225m and stretched
 165 vertical levels below 225m. The horizontal grids are formulated in spherical coordinates and
 166 vertical grids are in z levels. The model employs a B-grid structure in which the velocities are
 167 resolved at corners of the tracer grids. The model uses a centered-in-space and centered-in-time
 168 (CSCT) numerical scheme along with an Asselin-Robert filter (Asselin, 1972) to control the
 169 ripples in CSCT.

170 The tracer concentration (C) evolves with time as

$$171 \quad \frac{\partial C}{\partial t} + U \cdot \nabla_H C + W \frac{\partial C}{\partial z} = \frac{\partial}{\partial z} K_z \frac{\partial C}{\partial z} + \nabla_H \cdot (K_h \nabla_H C) + J + F \quad (1)$$

172 where ∇_H is the horizontal gradient operator, U and W are the horizontal and vertical velocities
 173 respectively. K_z is the vertical mixing coefficient, and K_h is the two-dimensional diffusion
 174 tensor. J represents any sink or source due to the internal consumption or production of the
 175 tracer. F represents the emission or absorption of fluxes at the ocean surface. Here, the source
 176 and sink terms are provided through the biogeochemical model. Vertical mixing is resolved in
 177 the model using K- profile parameterization (KPP) (Large et al., 1994).

178 In addition to KPP, the model uses a background vertical diffusion reported by Bryan and Lewis
 179 (Bryan and Lewis, 1979). For horizontal mixing, model incorporates Redi fluxes (Redi, 1982)

180 and GM fluxes (Gent and McWilliams, 1990) which represent the eddy-induced variance in the
181 mean tracer transport. A weak Laplacian diffusion is also included in the model for
182 computational stability where the sharp gradient in concentration occurs.

183 **2.2. Biogeochemical model**

184 The biogeochemical model used in the study is based on the OCMIP – II protocol as
185 stated above. The main motivation of OCMIP–II protocol is to employ a minimalistic approach
186 to simulate the ocean carbon cycle with a nutrient restoration approach to calculate the oceanic
187 biological production (Najjar et al., 1992; Anderson and Sarmiento, 1995). The present version
188 of the model has four prognostic variables coupled with the circulation field, viz., inorganic
189 phosphate (PO_4^{3-}), dissolved organic phosphorus (DOP), dissolved inorganic carbon (DIC) and
190 alkalinity (ALK). The basic currency for the biological model is phosphorous because of the
191 availability of a more extensive phosphate database and to eliminate the complexities associated
192 with nitrogen fixation and denitrification. Detailed model equations and variables are provided in
193 Appendix-A with only a brief description given below.

194 The production of organic phosphorus in the model using the nutrient restoring approach is given
195 by

$$196 \quad J_{prod} = \frac{1}{\tau} ([PO_4] - [PO_4]^*) \quad (2)$$

$$197 \quad [PO_4] > [PO_4]^* ; Z < Z_c$$

$$198 \quad J_{prod} = 0 \quad (3)$$

$$199 \quad [PO_4] \leq [PO_4]^*$$

200 Where J_{prod} represents the biogeochemical flows with respect to production of organic
201 phosphorous. $[PO_4]^*$ is the observed phosphate concentration and $\tau=30$ days is the restoration
202 time scale (Najjar et. al., 1992).

203 The vertically integrated new production ($g\ C\ m^{-2}\ yr^{-1}$) in the model is defined as

$$New\ production = \int_{z_c}^0 -J_{prod}\ dz \quad (4)$$

204 The export production ($g\ C\ m^{-2}\ yr^{-1}$) in the model is calculated as

$$Export\ production = (1 - \sigma) \int_0^{z_c} J_{prod}\ dz \quad (5)$$

205 Air-sea CO_2 flux in the model is estimated by,

$$F = K_w \Delta pCO_2 \quad (6)$$

207 where K_w is gas transfer velocity and ΔpCO_2 is the difference in partial pressure of carbon
208 dioxide between the ocean and atmosphere.

209 pCO_2 is calculated in the model by using DIC and ALK and is given by,

$$pCO_2 = \frac{[DIC]}{K_0} \frac{[H^+]^2}{[H^+]^2 + K_1[H^+] + K_1K_2} \quad (7)$$

210 Where $[H^+]$ is calculated using Newton-Raphson iterative method (Press et. al., 1996, Najjar and
211 Orr, 1998). K_0 is the solubility constant of CO_2 and K_1, K_2 are the dissociation constant for
212 carbonic acid, respectively (Sarmiento and Gruber, 2006, Weiss, 1974, Mehrbach et al., 1973,
213 Dickson and Millero, 1987, Najjar and Orr, 1998).

214 Details of all parameters in the biogeochemical model and calculations of solubility and
215 biological pump are listed in Appendix-A. The design and validation of the physical model is
216 reported by Valsala et al., (2008, 2010b) and biogeochemical model by Najjar and Orr (1998).

217

218 **2.3. Data**

219 For validating the model results, observational datasets of CO₂ flux and pCO₂ are taken
220 from Takahashi et al., (2009). Satellite-derived NPP data were taken from Sea-viewing Wide
221 Field of view Sensor (SeaWiFS) Chl-a product, calculated using Vertically Generalized
222 Production Model (VGPM) (Behrenfeld and Falkowski, 1997). The NPP data is scaled to export
223 production (EP) by multiplying with an e-ratio ($e = 0.37$) representative of Indian Ocean
224 upwelling zones (Sarmiento and Gruber, 2006, Laws et al., 2000; Falkowski et al., 2003). The
225 initial conditions for PO₄ are taken from the World Ocean Atlas (Garcia et al., 2014). Initial
226 conditions for DIC and ALK are taken from the Global Ocean Data Analysis Project (GLODAP;
227 Key et al., 2004) dataset. The dissolved Organic Phosphorous (DOP) is initialized with a
228 constant value of 0.02 $\mu\text{mol kg}^{-1}$ (Najjar and Orr, 1998). The data sources and citations are
229 provided in the Acknowledgement.

230

231 **2.4. Methods**

232 A spin-up for 50 years from the given initial conditions is performed with the
233 climatological physical drivers. As the initial conditions are provided from a mean state of
234 observed climatology, this duration of spin-up is sufficient to reach statistical equilibrium in the

235 upper 1000 m (Le Quere et al., 2000). Atmospheric pCO₂ has been set to a value from the 1950s
236 in the spin-up run for calculating the air-sea CO₂ exchange. A seasonal cycle of atmospheric
237 pCO₂ has been prescribed as in Keeling et al. (1995).

238 After the spin-up, an interannual simulation for 50 years from 1961 to 2010 has been
239 carried out with the corresponding observed atmospheric pCO₂ described in Keeling et al.,
240 (1995). The first five years of the interannual run were looped five times through the physical
241 fields of 1961 repeatedly for a smooth merging of the spin-up restart to the interannual physical
242 variables. Since the study is focused on bias corrections to the seasonal cycle of pCO₂ and DIC
243 with a variable Z_c, a model climatology for carbon cycle has been constructed from 1990 to
244 2010, which includes the anthropogenic increase of oceanic DIC in the climatological calculation
245 and is comparable with the Takahashi et al. (2009) observations.

246 Additional two sensitivity experiments have been performed separately by providing
247 annual mean currents or temperatures as drivers over selected regions of the basin in order to
248 segregate the role of varying Z_c in improving the seasonality of carbon cycle. The aim of these
249 sensitivity experiments is to understand how successful the new parameterization for Z_c is in
250 capturing the carbon cycle variability related to the upwelling episodes even though the seasonal
251 cycle in physics is suppressed. The model driven with annual mean currents suppresses the
252 effect of upwelling by muting the Ekman divergence over the region of interest. On the other
253 hand, the model forced with annual mean temperatures suppresses the cooling effect of
254 upwelling. A smoothing technique with linear interpolation ($u = u(1 - x) + \bar{u}x$) is applied to
255 the offline-data in order to blend the annual mean fields (\bar{u}) provided to the selected region with
256 the rest of the domain (u) in order to reduce a sudden transition at the boundaries. Here x
257 represents an index which varies between 0 and 1 within a distance of 10^0 from the boundaries of

258 the region of interest to the rest of the model domain. Results of sensitivity experiments are
259 provided in supplementary material.

260

261 **2.5. Community compensation depth (Z_c) parameterization**

262 The OCMIP – II protocol separates the production and consumption zones by a depth termed
263 as compensation depth (Z_c); the depth at which photosynthesis is large enough to balance the
264 community respiration (i.e., both the autotrophic and heterotrophic respiration). At the
265 community compensation depth, the NCP is zero i.e., $NCP = NPP - R_h = 0$, (i.e., $NPP = GPP -$
266 R_a), GPP is gross primary production, and R_h and R_a are the heterotrophic and autotrophic
267 respirations, respectively (Smetacek and Passow, 1990; Najjar and Orr, 1998; Gattuso et al.,
268 2006; Regaudix-de-Gioux and Duarte, 2010; Marra et al., 2014). The light intensity at Z_c is
269 compensation irradiance (E_{com}), the irradiance at which the gross community primary production
270 balances respiratory carbon losses for the entire community (Gattuso et al., 2006; Regaudix-de-
271 Gioux and Duarte, 2010). We define a spatially and temporally varying compensation depth
272 (hereafter $varZ_c$) as a depth where compensation irradiance (attenuated by surface Chl-a, Jerlov
273 et al., 1976) reaches a minimum value of 10 W m^{-2} . In this way, the $varZ_c$ has both spatio-
274 temporal variability of light as well as Chl-a. The Chl-a is given as monthly climatology as
275 constructed from satellite data. Observations show that the primary production reduces rapidly to
276 20% or less of the surface value below a threshold of 10 W m^{-2} (Parsons et al., 1984; Ryther,
277 1956; Sarmiento and Gruber, 2006). Moreover higher ocean temperatures (those in the tropics)
278 enhance the respiration rates resulting in high compensation irradiance (Parsons et al., 1984;
279 Ryther, 1956; Lopez-Urrutia et al., 2006; Regaudix-de-Gioux and Duarte, 2010). A study by

280 Regaudix-de-Gioux and Duarte (2010) reported the mean value of compensation irradiance over
281 the Arabian Sea as $0.4 \pm 0.2 \text{ mol photon m}^{-2} \text{ day}^{-1}$ which is close to $10 \text{ W m}^{-2} \text{ day}^{-1}$.

282 Figure 2 compares the scatter of average relative photosynthesis within varZc as a
283 function of solar radiation for the Indian Ocean (see Appendix-B). This encapsulates the
284 corresponding curve from the observations for the major phytoplankton species in the ocean such
285 as diatoms, green algae and dinoflagellates (Ryther et al., 1956; Parsons et al., 1984; Sarmiento
286 and Gruber, 2006). The model permits 100% production of organic phosphorus for radiation
287 above 10 W m^{-2} . However the availability of phosphate concentration in the model acts as an
288 additional limit for production which indirectly represents the photoinhibition at higher
289 irradiance; for example, in the oligotrophic gyres.

290

291 3. Results and Discussions

292 The inclusion of seasonality in Zc by way of parameterizing varZc leads to a remarkable
293 spatio-temporal variability in Zc (Figure 3). Zc over the Arabian Sea varies from 10 m to 25 m
294 during December to February (DJF) and deepens down to 45 m during March to May (MAM)
295 due to the increase in the surface solar radiation. During the monsoon season i.e., June to
296 September (JJAS), Zc again shoals to 10 m - 35 m due to the attenuation of solar radiation by the
297 increased biological production (Chl-a). During October to November (ON), Zc slightly deepens
298 as compared to JJAS.

299 The Bay of Bengal Zc deepens from 35 m to 40 m during DJF and further deepens to 50 m
300 during MAM when the solar radiation is maximum and biological production is minimum

301 (Prasannakumar et al., 2002). Further reduction of Z_c can be seen through JJAS as a result of a
302 reduction in solar radiation during monsoon cloud cover. Z_c during ON is 35 m on average.

303 The equatorial Indian Ocean can be seen as a belt of 40 m - 45 m Z_c throughout the season
304 except for JJAS. During JJAS, a shallow Z_c is seen near the coastal Arabian Sea (around 10 m to
305 35 m) presumably due to the coastal Chl-a blooms. Deep Z_c off the coast of Sumatra (~ 40 m to
306 50 m) is found during JJAS. Java-Sumatra coastal upwelling is centered on SON (Susanto et al.,
307 2001) and upwelling originates at around 100 m depth (Valsala and Maksyutov, 2010a; Xing et
308 al., 2012).

309 Southward of 10°S in the oligotrophic gyre region, Z_c varies from 40 m to more than 60 m
310 throughout the year. A conspicuous feature observed while parameterizing the solar radiation
311 and Chl-a dependent Z_c is that its maximum value never crosses 75 m especially in the Indian
312 Ocean which is the value specified in OCMIP-II models. The cutoff depth of 75 m in OCMIP-II
313 is obtained from observing the seasonal variance in oxygen data (Najjar and Keeling, 1997) as an
314 indicator of the production zone. However, our results show that parameterizing a production
315 zone based on solar radiation and Chl-a predicts a production zone and its variability that is
316 largely less than 75 m. The relevance of $\text{var}Z_c$ in the seasonality of the modeled carbon cycle is
317 illustrated as follows.

318

319 **3.1. Simulated seasonal cycle of pCO_2 and CO_2 fluxes**

320 The annual mean biases in simulated CO_2 fluxes and pCO_2 were evaluated by comparing
321 with Takahashi et al., (2009) observations (Figure 4). The model biases are significantly reduced

322 with the implementation of varZc compared to that of the constant Zc (hereinafter constZc). A
323 notable reduction in pCO₂ bias (by ~ 10µatm) is observed along the WAS (Figure 4d).

324 In order to address the role of the new biological parameterization of a variable Zc, we
325 zoom in on four key regions where the biological production and CO₂ fluxes are prominent in the
326 Indian Ocean with additional sensitivity experiments (see Introduction and references therein).
327 The regions (boxes shown in Figure 1) we considered are, (1) Western Arabian Sea (WAS;
328 40°E:65°E, 5°S:25°N) (2) Sri Lanka Dome (SLD; 81°E:90°E, 0°:10°N) (3) Seychelles-Chagos
329 Thermocline Ridge (SCTR; 50°E:80°E, 5°S:10°S) and (4) Sumatra Coast (SC; 90°E:110°E,
330 0°:10°S; Figure 1). The seasonal variations of Zc over these selected key regions are shown in
331 Figure 5. A detailed analysis of CO₂ fluxes, pCO₂, biological export and new productions and the
332 impact of varZc simulations in improving the strength of biological pump and solubility pump
333 for these key regions are presented below.

334

335 **3.2. Western Arabian Sea (WAS)**

336 The WAS Zc has a double peak pattern over the annual cycle. During the February-March
337 period, Zc deepens down to a maximum of 43.85 ± 2.3 m into March and then shoals to $25.75 \pm$
338 1.5 m (Figure 5) during the monsoon period (uncertainty represents the interannual standard
339 deviations of monthly data from 1990-2010). This shoaling of Zc depth during the monsoon
340 indicates the potential ability of the present biological parameterization to capture the wind-
341 driven upwelling related production in the WAS. During the post-monsoon period, the second
342 deepening of Zc occurs during November with a maximum depth of 34.91 ± 2.2 m. The ability to
343 represent the seasonality of the production zone renders a unique improvement in CO₂ flux

344 variability especially in the WAS in comparison to the OCMIP-II experiments (Orr et al, 2003;
345 Figure 6a).

346 OCMIP –II simulations with a constZc of 75 m underestimate the CO₂ flux when compared
347 to the observations of Takahashi et al. (2009). This underestimation is clearly visible during the
348 monsoon period. Our simulations with the varZc result in a better seasonality of CO₂ flux when
349 compared with Takahashi et al. (2009) observations (Figure 6a). The improvement due to the
350 varZc scheme is able to represent the seasonality of CO₂ flux better especially during the
351 monsoon period when wind-driven upwelling is dominant. Obviously, the relative role of the
352 biological and solubility pumps have to be deciphered in this context.

353 The CO₂ flux during July from observations, constZc, and varZc simulations are 3.09 mol m⁻²
354 yr⁻¹, 1.82 ± 0.4 mol m⁻² yr⁻¹ and 3.10 ± 0.5 mol m⁻² yr⁻¹, respectively. Southwesterly wind-driven
355 upwelling over the WAS especially off the Somali coast (Smith and Codispoti, 1980; Schott,
356 1983; Smith, 1984) and Oman (Bruce, 1974; Smith and Bottero, 1977; Swallow, 1984; Bauer et
357 al., 1991), pulls nutrient-rich subsurface waters closer to the surface while the available turbulent
358 energy due to the strong winds lead to mixed layer entrainment of the nutrients resulting in a
359 strong surface phytoplankton bloom (Krey and Babenerd, 1976; Banse, 1987; Bauer, 1991;
360 Brock et al, 1991). This regional bloom extends over 700 km offshore from the Omani coast due
361 to upward Ekman pumping driven by strong, positive wind-stress curl to the northwest of the low
362 level jet axis and the offshore advection (Bauer et al., 1991; Brock et al., 1991; Brock and
363 McClain, 1992a, b; Murtugudde and Busalacchi, 1999, Valsala, 2009) resulting in strong
364 outgassing of CO₂ flux and an enhanced pCO₂ in the WAS (Valsala and Maksyutov, 2013;
365 Sarma et al., 2002). The seasonal mean CO₂ flux during the southwest monsoon period (JJAS)
366 for constZc and varZc simulations are 1.44 ± 0.2 mol m⁻² yr⁻¹ and 2.31 ± 0.4 mol m⁻² yr⁻¹,

367 respectively. The biological parameterization of varZc considerably improves the average CO₂
368 flux during the monsoon period by $0.86 \pm 0.1 \text{ mol m}^{-2} \text{ yr}^{-1}$. The annual mean CO₂ flux from
369 observations, constZc and varZc simulations are $0.94 \text{ mol m}^{-2} \text{ yr}^{-1}$, $0.80 \pm 0.17 \text{ mol m}^{-2} \text{ yr}^{-1}$ and
370 $1.07 \pm 0.2 \text{ mol m}^{-2} \text{ yr}^{-1}$, respectively. The annual mean CO₂ flux is improved by $0.27 \pm 0.05 \text{ mol}$
371 $\text{m}^{-2} \text{ yr}^{-1}$.

372 Seasonality in pCO₂ also shows a remarkable improvement during the southwest monsoon
373 period (Figure 6b). The pCO₂ with constZc is considerably lower at a value of $385.22 \pm 3.5 \text{ } \mu\text{atm}$
374 during June compared to observational values of $392.83 \text{ } \mu\text{atm}$. However, varZc simulation
375 performs better in terms of pCO₂ variability. The peak value of pCO₂ reaches up to 405.42 ± 5.8
376 μatm . The seasonal mean pCO₂ during the Southwest monsoon period from observations,
377 constZc, and varZc simulations are $397.58 \text{ } \mu\text{atm}$, $389.18 \pm 3.6 \text{ } \mu\text{atm}$ and $399.95 \pm 5.0 \text{ } \mu\text{atm}$,
378 respectively. The improvement in pCO₂ by varZc simulation is $10.76 \pm 1.3 \text{ } \mu\text{atm}$ when compared
379 with the constZc simulation. This clearly shows that constZc simulation fails to capture the pCO₂
380 driven by upwelling during the Southwest monsoon while the varZc simulation is demonstrably
381 better in representing this seasonal increase. The annual mean pCO₂ from observations, constZc,
382 and varZc simulations are $394.69 \text{ } \mu\text{atm}$, $389.62 \pm 3.9 \text{ } \mu\text{atm}$ and $391.19 \pm 4.7 \text{ } \mu\text{atm}$, respectively.
383 However, it is worth mentioning that there are parts of the year where the constZc performs
384 better compared to varZc. For instance, during MAM as well as in November, the constZc
385 simulation yields a better comparison with the observed pCO₂ whereas varZc simulation yields a
386 reduced magnitude of pCO₂. This may well indicate the biological vs. solubility pump controls
387 on pCO₂ during the intermonsoons. The role of mesoscale variability in the ocean dynamics may
388 also play a role (Valsala and Murtugudde, 2015). Nevertheless, during the most important season

389 (JJAS) when the pCO₂, CO₂ fluxes, and biological production are found to be dominant in the
390 Arabian Sea, the varZc produces a better simulation.

391 The improvements shown by the use of varZc in the simulation of CO₂ flux and pCO₂ can be
392 elicited by further analysis of the model biological production. Figure 7 shows the comparison of
393 model export production and new production with observational export production from
394 satellite-derived NPP for constZc and varZc simulations. The model export production in the
395 constZc simulation is much weaker when compared to varZc simulation. The varZc simulation
396 has improved the model export production. Theoretically, the new and export productions in the
397 model should be in balance with each other (Eppley and Peterson, 1979). The constZc export
398 production is much weaker than new production and it is not in balance. In contrast, the varZc
399 simulation yields a close balance among them.

400 Compared with the observational export production which peaks in August at a value of
401 154.78 g C m⁻² yr⁻¹, the varZc simulated export and new productions peak at a value of 160.44 ±
402 20.4 g C m⁻² yr⁻¹ and 167.18 ± 24.0 g C m⁻² yr⁻¹, respectively, but in July. A similar peak can be
403 observed in constZc simulated new production as well, with a value of 178.19 ± 28.0 g C m⁻² yr⁻¹.
404 This apparent shift of one month during JJAS in the model export production as well as in the
405 new production is noted as a caveat in the present set up which will need further investigation.
406 Arabian Sea production is not just limited by nutrients but also the dust inputs (Wiggert et al.,
407 2006). The dust-induced primary production in the WAS, especially over the Oman coast is
408 noted during August (Liao et al., 2016). The mesoscale variability in the circulation and its
409 impact on production and carbon cycle are also a limiting factor in this model as noted above.

410 The seasonal mean export production during the southwest monsoon period from satellite-
411 derived estimate is $123.57 \text{ g C m}^{-2} \text{ yr}^{-1}$, whereas for constZc and varZc simulations it is $84.81 \pm$
412 $16.0 \text{ g C m}^{-2} \text{ yr}^{-1}$ and $147.19 \pm 23.8 \text{ g C m}^{-2} \text{ yr}^{-1}$, respectively. The new biological
413 parameterization strengthens the model export production by $62.38 \pm 7.8 \text{ g C m}^{-2} \text{ yr}^{-1}$ for the
414 southwest monsoon period, which is over a 70% increase. This indicates a considerable impact
415 of the biological pump in the model simulated CO_2 flux and pCO_2 over the WAS. For constZc
416 simulation, the computed new production is slightly higher ($150.84 \pm 27.9 \text{ g C m}^{-2} \text{ yr}^{-1}$) than that
417 of varZc ($133.03 \pm 19.5 \text{ g C m}^{-2} \text{ yr}^{-1}$). The annual mean export production from observations,
418 constZc and varZc simulations are $94.31 \text{ g C m}^{-2} \text{ yr}^{-1}$, $77.41 \pm 15.1 \text{ g C m}^{-2} \text{ yr}^{-1}$ and 122.54 ± 25.2
419 $\text{g C m}^{-2} \text{ yr}^{-1}$, respectively.

420 To understand how the varZc parameterization strengthens the export production in the
421 model, we have analyzed the phosphate profiles. It appears that the varZc parameterization
422 allows more phosphate concentration (Figure 8a, b) in the production zone and thereby increases
423 the corresponding biological production (Figure 8c, d). The net export production in the model
424 during JJAS is consistent with the satellite data (Figure 7b). However, in the constZc case, the
425 exports are rather ‘flat’ throughout the season with a poor representation of seasonal biological
426 export. The Table 1-4 summarize all the values discussed here.

427 The impact of varZc in the biological and solubility pumps is computed as per Louanchi et
428 al., (1996, see Appendix A). The varZc parameterization strengthens the biological as well as the
429 solubility pump in the model thereby modifying the phosphate profiles and achieves a seasonal
430 balance in export versus new production (Figure 9a). During the monsoon period, the varZc
431 simulation increases the strength of the solubility and biological pumps by $10.43 \pm 1.3 \text{ g C m}^{-2}$
432 yr^{-1} and $106.52 \pm 9 \text{ g C m}^{-2} \text{ yr}^{-1}$, respectively (see Table 5 and 6). Similarly, the annual mean

433 strength of solubility pump and the biological pump are increased by $3.29 \pm 0.6 \text{ g C m}^{-2} \text{ yr}^{-1}$ and
434 $81.18 \pm 9.92 \text{ g C m}^{-2} \text{ yr}^{-1}$, respectively. This supports the fact that the varZc parameterization
435 basically modifies the biological and solubility pumps in the model simulation and thereby
436 improves the seasonal cycle of CO_2 flux and pCO_2 .

437

438 **3.3 Sri Lanka Dome (SLD)**

439 The seasonal variation in Zc for SLD has a similar pattern as that of WAS. Zc deepens to its
440 maximum during March up to $45.23 \pm 0.3 \text{ m}$ and reaches its minimum during the following
441 monsoon period at $30.79 \pm 1.5 \text{ m}$ (Figure 5). The similarities of varZc between WAS and SLD
442 indicates that they both are under similar cycles of solar influx and biological production. The
443 SLD Chl-a dominates only up to July (Vinayachandran et al., 2004) which explains why
444 production with varZc increases earlier compared to WAS which occurs during ASO.

445 The seasonality in CO_2 flux and pCO_2 were compared with Takahashi et al., (2009)
446 observations (Figure 10). varZc results in a slight improvement in CO_2 flux when compared with
447 constZc (Figure 10a). However, both constZc and varZc simulations underestimate the
448 magnitude of CO_2 flux when compared with observations. The seasonal mean CO_2 flux during
449 the monsoon period is $1.79 \text{ mol m}^{-2} \text{ yr}^{-1}$ from observations, which means SLD region is a source
450 of CO_2 . But the mean values of constZc and varZc simulations yield flux values of -0.008 ± 0.2
451 $\text{mol m}^{-2} \text{ yr}^{-1}$ and $0.24 \pm 0.2 \text{ mol m}^{-2} \text{ yr}^{-1}$, respectively. The constZc simulation misrepresents the
452 SLD region as a sink of CO_2 during monsoon period which is opposite to that of observations.
453 The varZc simulation corrects this misrepresentation to a source albeit at a smaller magnitude by

454 $0.24 \pm 0.09 \text{ mol m}^{-2} \text{ yr}^{-1}$ for the monsoon period. Compared to observations, the varZc case
455 underestimates the magnitude of JJAS mean by $1.55 \text{ mol m}^{-2} \text{ yr}^{-1}$.

456 The annual mean CO_2 fluxes for constZc and varZc simulations are $-0.02 \pm 0.1 \text{ mol m}^{-2} \text{ yr}^{-1}$
457 and $0.10 \pm 0.2 \text{ mol m}^{-2} \text{ yr}^{-1}$, respectively. The varZc parameterization leads to an improvement of
458 $0.13 \pm 0.1 \text{ mol m}^{-2} \text{ yr}^{-1}$ in the annual mean CO_2 flux when compared with constZc simulation.
459 The observational annual mean of CO_2 flux is $0.80 \text{ mol m}^{-2} \text{ yr}^{-1}$ which is highly underestimated
460 by both simulations. This indicates a regulation of biological production of the region by varZc
461 which makes this region a source of CO_2 during monsoon. The role of the solubility pump may
462 also be underestimated due to the biases in the physical drivers and the lack of mesoscale eddy
463 activities in these simulations (Prasanna Kumar et al., 2002; Valsala and Murtugudde, 2015).

464 The seasonality of pCO_2 (Figure 10b) especially in the monsoon period is significantly
465 improved. The mean pCO_2 during the monsoon season from observation over the SLD region is
466 $382.44 \text{ } \mu\text{atm}$. The seasonal mean pCO_2 during monsoon period for constZc and varZc
467 simulations are $371.67 \pm 6.04 \text{ } \mu\text{atm}$ and $379.24 \pm 8.9 \text{ } \mu\text{atm}$, respectively. The annual mean pCO_2
468 from observations, constZc, and varZc simulations are $380.21 \text{ } \mu\text{atm}$, $370.76 \pm 6.1 \text{ } \mu\text{atm}$ and
469 $374.94 \pm 9.6 \text{ } \mu\text{atm}$, respectively. varZc simulations improve the JJAS mean pCO_2 by 7.56 ± 2.8
470 μatm and the annual mean pCO_2 by $4.18 \pm 3.5 \text{ } \mu\text{atm}$, which is reflected in CO_2 flux as well. This
471 is likely due to the impact of new biological parameterization in capturing the episodic upwelling
472 in the SLD region which is further investigated by looking at its biological production.

473 The SLD biological production is highly exaggerated by the model for both constZc and
474 varZc simulations (Figure 11a, b). The seasonal mean biological export for the monsoon period
475 is $51.54 \text{ g C m}^{-2} \text{ yr}^{-1}$ as per satellite-derived estimates. However, the constZc and varZc

476 simulations overestimate it at $167.71 \pm 59.04 \text{ g C m}^{-2} \text{ yr}^{-1}$ and $151.51 \pm 46.4 \text{ g C m}^{-2} \text{ yr}^{-1}$,
477 respectively. This exaggerated export is visible in climatological annual means where for
478 constZc and varZc simulations they are $144.43 \pm 49.8 \text{ g C m}^{-2} \text{ yr}^{-1}$ and $156.08 \pm 43.8 \text{ g C m}^{-2} \text{ yr}^{-1}$,
479 respectively.

480 For constZc simulation, new production is overestimated from March to October when
481 compared to observations and the second peak is observed in November (Figure 11a). But the
482 overestimate in new production with varZc is observed only during JJAS period by an amount of
483 $26.23 \text{ g C m}^{-2} \text{ yr}^{-1}$. For the SLD region, the varZc parameterization overestimates the export
484 production but minimizes the excess new production, especially in the monsoon period by 64.15
485 $\pm 36.4 \text{ g C m}^{-2} \text{ yr}^{-1}$. This indicates that the varZc parameterization is somewhat successful in
486 capturing the upwelling episode during the monsoon over SLD. All values are summarized in
487 Tables 1 to 4.

488 The solubility and biological pumps are modified by the varZc parameterization significantly
489 when compared with the constZc simulation (Figure 9b). Over the monsoon period, the strength
490 of the solubility and biological pumps are improved by $2.81 \pm 1.1 \text{ g C m}^{-2} \text{ yr}^{-1}$ and $66.68 \pm 9.7 \text{ g}$
491 $\text{C m}^{-2} \text{ yr}^{-1}$, respectively. Similarly, the annual mean strength of solubility and biological pump
492 are increased by $0.99 \pm 1.2 \text{ g C m}^{-2} \text{ yr}^{-1}$ and $52.5 \pm 5.1 \text{ g C m}^{-2} \text{ yr}^{-1}$ respectively. All values are
493 provided in Table 5 and 6.

494

495 **3.4 Sumatra Coast (SC)**

496 The seasonal variation in Zc over the SC region lies between 40 m and 46 m (Figure 5). The
497 seasonal maximum occurs during JFM, especially in March with a depth of 45.5 m. During the

498 monsoon period, Z_c shoals slightly with a minimum of 41.1 m in July. The variation in Z_c is
499 relatively small as compared to the other regions which is consistent with its relatively low
500 production throughout the year.

501 The seasonality of CO_2 flux and pCO_2 captured by const Z_c and var Z_c simulations are shown
502 in Figure 12a, b. The var Z_c simulations overestimate both CO_2 flux and pCO_2 , especially during
503 the monsoon. It is found that the const Z_c simulation is better compared to var Z_c simulation. The
504 var Z_c simulation overestimates the seasonal mean CO_2 flux and pCO_2 by $1.19 \text{ mol m}^{-2} \text{ yr}^{-1}$ and
505 $29.61 \text{ } \mu\text{atm}$, respectively, compared to observations (Table 1). However, const Z_c produces a
506 better estimate compared with observations for CO_2 flux and pCO_2 . The const Z_c simulation also
507 delivers a better annual mean than var Z_c (Table 1, 2). The annual mean bias in const Z_c and
508 var Z_c simulations for CO_2 flux is $-0.0033 \text{ mol m}^{-2} \text{ yr}^{-1}$ and $0.31 \text{ mol m}^{-2} \text{ yr}^{-1}$, respectively.
509 Similarly, pCO_2 bias is $1.95 \text{ } \mu\text{atm}$ and $9.07 \text{ } \mu\text{atm}$ for const Z_c and var Z_c simulations.

510 Biological production simulated by the model along SC explains the overestimation of CO_2
511 flux and pCO_2 (Figure 13). Both const Z_c and var Z_c simulations greatly overestimate export
512 production in the model. However, a small enhancement in the new production during JJAS in
513 const Z_c case is an indicator of upwelling episodes. The seasonal mean new production during
514 the monsoon from const Z_c and var Z_c are $63.64 \pm 30.9 \text{ g C m}^{-2} \text{ yr}^{-1}$ and $78.11 \pm 29.1 \text{ g C m}^{-2} \text{ yr}^{-1}$,
515 respectively (Table 4). The seasonal mean export production during the monsoon from
516 observations is $58.87 \text{ g C m}^{-2} \text{ yr}^{-1}$ (Table 3). The const Z_c simulation represents a better new
517 production, which is seen as a relatively small exaggeration of CO_2 flux and pCO_2 . The
518 biological response of SC is found to be better with const Z_c which is in contradiction to a
519 general improvement found with var Z_c in the other regions examined here. Such discrepancies
520 over the SC could be due to the effect of Indonesian Throughflow (Bates et al., 2006) which is

521 not completely resolved in the model due to coarse spatial resolution (also see Valsala and
522 Maksyutov, 2010a).

523 The overestimation of export production by varZc simulation is also evident by the increase
524 in strength of the biological and solubility pumps, respectively (Figure 9c). The annual mean and
525 JJAS mean DIC increases in the production zone due to the biological pump are $67.21 \pm 1.3 \text{ g C}$
526 $\text{m}^{-2} \text{ yr}^{-1}$ and $83.62 \pm 0.5 \text{ g C m}^{-2} \text{ yr}^{-1}$, respectively. Similarly the increase in DIC due to the effect
527 of solubility pump during the JJAS period and annual mean are $10.95 \pm 5.2 \text{ g C m}^{-2} \text{ yr}^{-1}$ and 3.87
528 $\pm 2.2 \text{ g C m}^{-2} \text{ yr}^{-1}$ respectively (see table 5 and 6).

529

530 **3.5 Seychelles-Chagos Thermocline Ridge (SCTR)**

531 The SCTR is a unique open-ocean upwelling region with a prominent variability in air-sea
532 interactions (Xie et al., 2002). Wind-driven mixing and upwelling of subsurface nutrient-rich
533 water play a major role in the biological production of this region (Dilmahamod et al., 2016).
534 The seasonal cycle in Zc is shown in Figure 5. The maximum Zc occurs in November at about
535 44.94 m and the minimum at 33.2 m in July. The shoaling of Zc during the monsoon period
536 shows that the biological parameterization captures the response to upwelling over this region.

537 The seasonality of CO₂ flux and pCO₂ are shown in Figure 14. The Takahashi observations
538 of CO₂ flux show a peak in June with outgassing of CO₂ during the upwelling episodes.
539 However, both constZc and varZc simulations underestimate this variability. The seasonality of
540 CO₂ flux in varZc shows a significant improvement when compared to constZc simulation, but
541 underestimated when compared to observations. The seasonal mean CO₂ flux during the
542 monsoon from observations, constZc and varZc simulations are $0.82 \text{ mol m}^{-2} \text{ yr}^{-1}$, -0.32 ± 0.3

543 mol m⁻² yr⁻¹ and -0.05 ± 0.4 mol m⁻² yr⁻¹, respectively. This represents a reduction in the seasonal
544 mean sink of CO₂ flux in the SCTR region during the monsoon by 0.27 ± 0.1 mol m⁻² yr⁻¹
545 bringing it closer to a source region (see Table 1 for details).

546 The improved CO₂ flux is also supported by the seasonal cycle in pCO₂. Based on
547 observations, the seasonal mean of pCO₂ with constZc during JJAS is underestimated by 11.47
548 μatm, varZc simulation underestimates it by 6.45 μatm. So it is evident that varZc simulation
549 capture the upwelling episodes better, marked by a larger pCO₂ during JJAS period. However,
550 the magnitude of pCO₂ is still underestimated compared to observations (Table 2).

551 Figure 15 shows the biological production of constZc and varZc simulations for SCTR. It is
552 clear that both simulations overestimate the export production and underestimate the new
553 production. The JJAS mean export production from observations, constZc and varZc are 51.08 g
554 C m⁻² yr⁻¹, 57.39 ± 14.2 g C m⁻² yr⁻¹ and 99.23 ± 29.8 g C m⁻² yr⁻¹, respectively. The varZc
555 simulations exaggerate the model export production by 48.14 g C m⁻² yr⁻¹. The varZc simulation
556 improves the JJAS mean new production by 1.14 ± 2.2 g C m⁻² yr⁻¹ (Table 4). The DIC variations
557 due to the biological pump over the monsoon period and the annual mean also correspond to the
558 exaggerated export production. During the monsoon period, the varZc simulation strengthens the
559 biological and solubility pumps by 72.64 ± 6.2 g C m⁻² yr⁻¹ and -4.56 ± 1.6 g C m⁻² yr⁻¹,
560 respectively, when compared to the constZc simulation (Figure 9d). This is also reflected in the
561 annual mean DIC variations due to the biological and solubility pump effects (see table 5 and 6).
562 This slight improvement in the model new production, especially during the monsoon period
563 signals that the varZc better captures the upwelling over SCTR. Considering the annual mean
564 values of model export and new production, constZc simulation is reasonably faithful to
565 observations.

566 The underestimation of CO₂ and pCO₂, as well as the exaggeration of model export
567 production and a slight, overestimate in model new production may be due to two reasons; (1)
568 SCTR is a strongly coupled region with remote forcing of the mixed layer – thermocline
569 interactions (Zhou et al., 2008) which can affect the seasonality in biological production that the
570 model may not be resolving reasonably, (2) the bias associated with physical drivers, especially
571 wind stress may underestimate the CO₂ flux as well biological production. A similar
572 overestimation of biological production was also reported in a coupled biophysical model
573 (Dilmahamod et al., 2016).

574 Table 1 – 4 shows the entire summary of seasonal and annual mean CO₂ flux, pCO₂ and
575 biological production reported in Section 3.

576

577 **4. Summary and Conclusions**

578 A spatially and temporally varying Zc parameterization as a function of solar radiation and
579 Chl-a is implemented in the biological pump model of OCMIP-II for a detailed analysis of
580 biological fluxes in the upwelling zones of the Indian Ocean. The varZc parameterization
581 improves the seasonality of model CO₂ flux and pCO₂ variability, especially during the monsoon
582 period. A significant improvement is observed in WAS where the monsoon wind-driven
583 upwelling dominates biological production. The magnitude of CO₂ flux matches with
584 observations, especially in July when monsoon winds are at their peak. Monsoon triggers
585 upwelling in SLD as well which acts as a source of CO₂ to the atmosphere. The seasonal and
586 annual mean are underestimated with constZc and the SLD is reduced to a sink of CO₂ flux. The
587 varZc simulation modifies the seasonal and annual means of the CO₂ flux of SLD and depict it as

588 a source of CO₂ especially during the monsoon, but the magnitude is still underestimated
589 compared to Takahashi et al. (2009) observations. The SCTR variability is underestimated by
590 both constZc and varZc simulations, portraying it as a CO₂ sink region whereas observations
591 over the monsoon period indicate that the thermocline ridge driven by the open ocean wind-
592 stress curl is, in fact, an oceanic source of CO₂. However, the varZc simulation reduces the
593 magnitude of the sink in this region bringing it relatively close to observations.

594 VarZc biological parameterization strengthens the export and new productions in the model,
595 which allows it to represent a better seasonal cycle of CO₂ flux and pCO₂ over the study regions.
596 The WAS export production is remarkably improved by $62.37 \pm 7.8 \text{ g C m}^{-2} \text{ yr}^{-1}$ compared to
597 constZc. This supports our conclusion that the varZc parameterization increases the strength of
598 biological export in the model. Over the SLD, the JJAS seasonal mean export and new
599 production are underestimated in varZc compared to constZc simulations, but the annual mean
600 export production is improved. Export production at SC and SCTR are highly exaggerated and
601 there is hardly any improvement in new production with a variable Zc especially over the
602 monsoon period. The inability of varZc parameterization to improve the seasonality of SC and
603 SCTR may be due to the interannual variability of biological production associated with the
604 Indonesian throughflow and remote forcing of the mixed layer-thermocline interactions and the
605 effect of biases in the wind stress data used as a physical driver in the model.

606 Sensitivity experiments carried out by prescribing annual mean currents or temperatures over
607 selected subdomains reveal that the varZc retains the seasonality of carbon fluxes, pCO₂, and
608 export and new productions closer to observations. This strongly supports our contention that
609 varZc parameterization improves export and new productions and it is also efficient in capturing
610 upwelling episodes of the study regions. This points out the significant role of having a close

611 balance in seasonal biological export and new production in models to capture the seasonality in
612 the carbon cycle. This also confirms the role of biological and solubility pumps in producing the
613 seasonality of carbon cycle in the upwelling zones.

614 However, the underestimation of the seasonality of CO₂ flux over the SLD and
615 overestimation over the SC as well as the SCTR are a cautionary flag for the study. This
616 uncertainty poses an important scientific question as to whether the model biology over the SC
617 and SCTR region is not resolving the seasonality in CO₂ flux and pCO₂ properly or whether the
618 seasonality in the Z_c is not able to fully capture the biological processes.

619 To address these questions we have used an inverse modeling approach (Bayesian inversion)
620 in order to optimize the spatially and temporally varying Z_c using surface pCO₂ as the
621 observational constraint and computed the optimized biological production. The results will be
622 reported elsewhere.

623

624

625

626

627

628

629

630

631 **Appendix – A**

632 The time evolution equations of the model variables are given by

$$\frac{d[PO_4]}{dt} = L([PO_4]) + J_{PO_4} \quad (A1)$$

$$\frac{d[DOP]}{dt} = L([DOP]) + J_{DOP} \quad (A2)$$

$$\frac{dDIC}{dt} = L([DIC]) + J_{DIC} + J_g DIC + J_v DIC \quad (A3)$$

$$\frac{d[ALK]}{dt} = L([ALK]) + J_{ALK} + J_v ALK \quad (A4)$$

633 Where L is the 3D transport operator, which represents the effects of advection, diffusion, and
 634 convection. [] or square brackets indicate the concentrations in mol m⁻³. $J_{PO_4}, J_{DOP}, J_{DIC}, J_{ALK}$
 635 are the biological source/sink terms and $J_v DIC, J_v ALK$ are the virtual source-sink terms
 636 representing the changes in surface DIC and ALK, respectively, due to evaporation and
 637 precipitation. $J_g DIC$ is the source-sink term due to air-sea exchange of CO₂.

638 The following equations represent for the biological processes in the model

639 For $Z < Z_c$,

$$640 J_{prod} = \frac{1}{\tau}([PO_4] - [PO_4^*]), \quad [PO_4] > [PO_4^*] \quad (A5)$$

$$641 J_{DOP} = \sigma J_{prod} - \kappa[DOP] \quad (A6)$$

$$642 J_{PO_4} = -J_{prod} + \kappa[DOP] \quad (A7)$$

$$643 \quad J_{ca} = Rr_{C:P}(1 - \sigma)J_{prod} \quad (A8)$$

$$644 \quad J_{DIC} = r_{C:P}J_{PO4} + J_{ca} \quad (A9)$$

$$645 \quad J_{ALK} = -r_{N:P}J_{PO4} + 2J_{ca} \quad (A10)$$

646 For $Z > Z_c$,

$$647 \quad J_{prod} = 0, \quad [PO_4] \leq [PO_4^*] \quad (A11)$$

$$648 \quad J_{DOP} = -\kappa[DOP] \quad (A12)$$

$$649 \quad J_{PO4} = -\frac{\partial F}{\partial Z} + \kappa[DOP] \quad (A13)$$

$$650 \quad F_c = (1 - \sigma) \int_0^{Z_c} J_{prod} dZ \quad (A14)$$

$$651 \quad F(Z) = F_c \left(\frac{Z}{Z_c}\right)^{-a} \quad (A15)$$

$$652 \quad J_{ca} = -\frac{\partial F_{ca}}{\partial Z} \quad (A16)$$

$$653 \quad F_{ca} = Rr_{C:P}F_c e^{-(Z-Z_c)/d} \quad (A17)$$

654 Where Z is the depth and Z_c is the compensation depth in the model. J_{prod} , J_{ca} represents the
655 biogeochemical flows with respect to production and calcification. Within Z_c , the production of
656 organic phosphorous in the model J_{prod} is calculated using equation A5. $[PO_4]$ is the model
657 phosphate concentration and $[PO_4^*]$ is observational phosphate. τ is the restoration timescale
658 assumed to be 30 days. Whenever the model phosphate exceeds the observational phosphate, it
659 allows production, below which the production is zero. The observational phosphate data were
660 taken from the World Ocean Atlas (WOA; Garcia et al., 2014). It is assumed that a fixed fraction

661 (σJ_{prod}) of phosphate uptake is converted into Dissolved Organic Phosphorus (DOP) which is a
662 source for J_{DOP} (equation A6). The phosphate not converted to DOP results in an instantaneous
663 downward flux of particulate organic phosphorus at Z_c (equation A14). The decrease of flux
664 with depth due to remineralization is shown by a power law relationship as in equation A15. The
665 values of the constants a , κ , σ are 0.9, 0.2/year to 0.7/year, 0.67, respectively. The rate of
666 production is used to explain the formation of calcium carbonate cycle in surface waters
667 (equation A8) and its export is given by equation A16, where R is the rain ratio, a constant molar
668 ratio of exported particulate organic carbon to the exported calcium carbonate flux at Z_c . The
669 exponential decrease of calcium carbonate flux with scale depth d is given by equation A17. The
670 biological source or sink of dissolved inorganic carbon (DIC) and alkalinity (ALK) is explained
671 through equations A9 and A10, respectively. Where the values of rain ratio (R) is taken as 0.07
672 and the Redfield ratio, $r_{C:P} = 117$, and $r_{N:P} = 16$ and scale depth d is chosen as 3500m.

673

674 **Biological and Solubility Pump calculations**

675 The biological effect on DIC is calculated from Louanchi et al., (1996). The tendency of DIC
676 due to biomass production and calcite formation in the production zone is expressed as below.

$$677 \quad \left(\frac{\partial DIC}{\partial t}\right)_b = \left(\frac{\partial P O_4}{\partial t}\right)_b \times R_{C:P} - J_{Ca} \quad (A18)$$

678 The total tendency of DIC in the production zone is:

$$679 \quad \left(\frac{\partial DIC}{\partial t}\right)_{total} = \left(\frac{\partial DIC}{\partial t}\right)_b + \int_x \int_y F dx dy \quad (A19)$$

680 where $\left(\frac{\partial DIC}{\partial t}\right)_b$ is the evolution of DIC due to the impact of biology (i.e., biological pump). The
681 first term in the R.H.S of Equation A18 is the rate of change of phosphate resulting from
682 photosynthesis and respiration in the model (i.e., J_{po4} in this case) multiplied by the carbon to
683 phosphorous Redfield ratio ($R_{C:P} = 117:1$) and J_{Ca} represents the calcite formation in the model
684 (see Equation A8 & A16). The solubility pump is calculated as the surface integral of the flux F
685 (Louanchi et al., 1996).

686

687 **Appendix B**

688 In order to compare our model production of organic phosphorous to the curve of Ryther et al.,
689 (1956) we have merely scaled our total production to “relative photosynthesis”, which is,
690 according to Ryther et al., (1956) an index between 0 and 1 indicating the strength of production
691 estimated as P_l/P_{max} . Here P_l is the photosynthesis at each intensity (of light) of different species
692 and P_{max} is the maximum photosynthesis observed in the same control experiment. The curve
693 between relative photosynthesis and light intensity shows the relation between photosynthetic
694 activity and light in marine phytoplankton. Since our method relates biological production to a
695 function of light (limitation) by Chl-a attenuation, it is the best curve to cross-compare our
696 results. In this case we scaled our total biological production within Z_c into relative values
697 between 0-1 by P_l/P_{max} . in which P_l is taken as the individual grid cell biological component of
698 organic phosphorus production and P_{max} is the maximum production available in the domain at
699 any given instant. All the grid points are quite similar to the curve of Ryther et al., (1956) as
700 shown in Figure 2.

701

702 **Acknowledgements**

703 Thanks to two anonymous reviewers and the editor (Marilaure Grégoire) for comments. Sreesh
704 M. G. sincerely acknowledges the fellowship support from Indian Institute of Tropical
705 Meteorology (IITM) to carry out the study. The OCMIP-II routines were taken from
706 (<http://ocmip5.ipsl.jussieu.fr/OCMIP/>). GFDL data for OTTM is taken from
707 (<http://data1.gfdl.noaa.gov/nomads/forms/assimilation.html>). Takahashi data is taken from
708 (<http://www.ldeo.columbia.edu/res/pi/CO2/>) and SeaWiFS data is obtained from the National
709 Aeronautics and Space Administration (NASA) Ocean Color Website
710 (<http://oceancolor.gsfc.nasa.gov/>). The computations were carried out in High-Performance
711 Computing (HPC) facility of Ministry of Earth Sciences (MoES), IITM.

712

713

714

715

716

717

718

719

720

721 **References**

722 Anderson, L. A., Sarmiento, J. L.: Global ocean phosphate and oxygen simulations, *Global*
723 *Biogeochem. Cycles*, 9, 621-636, doi:10.1029/95GB01902, 1995.

724 Asselin, R.: Frequency filter for time integrations, *Mon. Wea. Rev.*, 100, 487–490, doi:
725 10.1175/1520-0493, 1972.

726 Banse, K., McClain, C. R.: Winter blooms of phytoplankton in the Arabian Sea as observed by
727 the Coastal Zone Color Scanner, *Mar. Ecol. Prog. Ser.*, 34, 201 – 211, 1986.

728 Banse, K.: Seasonality of phytoplankton chlorophyll in the central and northern Arabian Sea,
729 *Deep Sea Res.*, 34, 713 – 723, doi:10.1016/0198-0149, 1987.

730 Barber, R. T., Marra, J., Bidigare, R. C., Codispoti, L. A., Halpern, D., Johnson, Z., Latasa, M.,
731 Goericke, R., and Smith, S. L.: Primary productivity and its regulation in the Arabian Sea during
732 1995, *Deep. Sea. Res. pt. II*, 48, 1127 – 1172. doi:10.1016/S0967-0645, 2001.

733 Bates, N. R., Pequignet, A. C., and Sabine, C. L.: Ocean carbon cycling in the Indian Ocean: 2.
734 Estimates of net community production, *Global Biogeochem. Cycles.*, 20, GB3021,
735 doi:10.1029/2005GB002492, 2006.

736 Bauer, S., Hitchcock, G. L., Olson, D. B.: Influence of monsoonally-forced Ekman dynamics
737 upon surface-layer depth and plankton biomass distribution in the Arabian Sea, *Deep Sea Res.*,
738 38, 531 – 553, doi:10.1016/0198-0149, 1991.

739 Behrenfeld, M. J., Falkowski, P. G.: Photosynthetic rates derived from satellite-based
740 chlorophyll concentration, *Limnol. Oceanogr.*, 42, 1 – 20, doi: 10.4319/lo.1997.42.1.0001, 1997.

741 Boyd, P. W., Ryneerson, T. A., Armstrong, E. A., Fu, F., Hayashi, K. and co-authors.: Marine
742 Phytoplankton Temperature versus growth responses from polar to tropical waters – outcome of
743 a scientific community-wide study, PLoS ONE 8(5), e63091,
744 Doi:10.1371/journal.phone.0063091, 2013.

745 Brock, J C., McClain, C. R.: Interannual variability of the southwest monsoon phytoplankton
746 bloom in the north-western Arabian Sea, J. Geophys. Res., 97(C1), 733 – 750,
747 doi/10.1029/91JC02225, 1992a.

748 Brock, J. C., McClain, C. R., Hay, W. W.: A southwest monsoon hydrographic climatology for
749 the northwestern Arabian Sea, J. geophys. Res., 97(C6), 9455 – 9465, doi: 10.1029/92JC00813,
750 1992b.

751 Brock, J. C., McClain, C. R., Luther, M. E., Hay, W. W.: The phytoplankton bloom in the
752 northwestern Arabian Sea during the southwest monsoon of 1979, J. Geophys. Res., 96(C11),
753 623 – 642, doi: 10.1029/91JC01711, 1991.

754 Brock, J., Sathyendranath, S., and Platt, T.: Modelling the seasonality of subsurface light and
755 primary production in the Arabian Sea, Mar. Eco. Prog. Ser., 101, 209 – 221, 1993.

756 Bruce, J. G.: Some details of upwelling off the Somali and Arabian coasts, J. Mar. Res., 32, 419
757 – 423, 1974.

758 Bryan, K., Lewis, L. J.: A water mass model of the world ocean, J. Geophys. Res., 84, 2503 –
759 2517, doi: 10.1029/JC084iC05p02503, 1979.

760 Chang, Y. S., Zhang. S., Rosati. A., Delworth. T., Stern. W. F.: An assessment of oceanic
761 variability for 1960-2010 from the GFDL ensemble coupled data assimilation, *Clim. Dyn.*, 40,
762 775 – 803, doi: 10.1007/s00382-012-1412-2, 2012.

763 Christian J. R., Verschall M. A., Murtugudde R., Busalacchi A. J., McClain C. R.:
764 Biogeochemical modeling of the tropical Pacific Ocean. II: Iron biogeochemistry, *Deep Sea*
765 *Res.*, 49, 545 – 565, doi:10.1016/S0967-0645, 2001.

766 Colwell, R. R.: Global climate and infectious disease: the cholera paradigm, *Science.*, 274(5295),
767 2025 – 2031, doi: 10.1126/science.274.5295.2025, 1996.

768 Dickson, A. G., and F. J. Millero.: A comparison of the equilibrium constants for the dissociation
769 of carbonic acid in seawater media, *Deep-Sea Res.*, 34, 1733 – 1743, 1987.

770 Dilmahamod A. F., Hermes. J. C., Reason C. J. C.: Chlorophyll-a variability in the Seychelles-
771 Chagos Thermocline Ridge: Analysis of a coupled biophysical model, *J. of. Mar. Sys.*, 154, 220
772 – 232, doi:10.1016/j.jmarsys.2015.10.011, 2016.

773 Doney S. C., and co-authors.: Evaluating global ocean carbon models: The importance of
774 realistic physics, *Glob. Biogeochem. Cycles*, 18, doi:10.1029/2003GB002150, 2004.

775 Eppley, R. W., Peterson. B. J.: Particulate organic matter flux and planktonic new production in
776 the deep ocean, *Nature*, 282, 677-680, doi:10.1038/282677a0, 1979.

777 Eppley, R. W.: Temperature and phytoplankton growth in the sea, *Fish. Bull.*, 70, 1063 – 1085,
778 1972.

779 Falkowski, P. G., E. A. Laws, R. T. Barber, and J. W. Murray: phytoplankton and their role in
780 the primary, new and export production, In: Fasham M.J.R (eds) *Ocean Biogeochemistry*, Global

781 Change – The IGBP series (closed). Springer, Berlin, Heidelberg, doi:
782 https://doi.org/10.1007/978-3-642-55844-3_5, 2003.

783 Feely, R. A., Sabine, C. L., Takahashi, T., Wanninkhof, R.: Uptake and Storage of Carbon
784 Dioxide in the Ocean: The Global CO₂ Survey, *Oceanography.*, 14(4), 18–32,
785 doi:10.5670/oceanog.2001.03, 2001.

786 Friedrichs, M. A. M., and co-authors.: Assessment of skill and portability in regional
787 biogeochemical models: role of multiple planktonic groups, *J. Geophys. Res.*, 112, doi:
788 10.1029/2006JC003852, 2007.

789 Friedrichs, M. A. M., Hood, R. R., Wiggert, J. D.: Ecosystem complexity versus physical forcing
790 quantification of their relative impact with assimilated Arabian Sea data, *Deep Sea Res.*, 53, 576-
791 600, doi:10.1016/j.dsr2.2006.01.026, 2006.

792 Garcia, H. E., R. A. Locarnini, T. P. Boyer, J. I. Antonov, O.K. Baranova, M.M. Zweng, J.R.
793 Reagan, D.R. Johnson.: *World Ocean Atlas 2013, Volume 4: Dissolved Inorganic Nutrients*
794 (phosphate, nitrate, silicate), S. Levitus, Ed., A. Mishonov Technical Ed.; NOAA Atlas NESDIS
795 76, 25 pp, 2014.

796 Gattuso, J. P., B. Gentili, C. M. Duarte, J. A. Kleypas, J. J. Middelburg, and D. Antoine.: Light
797 availability in the coastal ocean: Impact on the distribution of benthic photosynthetic organisms
798 and their contribution to primary production, *Biogeosciences*, 3, 489 – 513, doi:10.5194/bg-3-
799 489-2006, 2006.

800 Gent, P. R., McWilliams. J. C.: Isopycnal mixing in ocean circulation models, *J. Phys.*
801 *Oceanogr.*, 20, 150 – 155, doi: 10.1175/15200485, 1990.

802 Harwell, C., Kim, K., Burkholder, J., Colwell, R., Epstein, P. R., Grimes, D., Hofmann, E. E.,
803 Lipp, E. K., Osterhaus, A., and Overshreet, R. M.: Emerging marine diseases-climate links and
804 anthropogenic factors, *Science.*, 285(5433), 1505 – 1510, doi: 10.1126/science.285.5433.1505,
805 1999.

806 Jerlov N. G.: *Marine optics*, Second ed., Elsevier, pp 231, 1976.

807 Jung, E., and Kirtman. B. P.: ENSO modulation of tropical Indian ocean subseasonal variability,
808 *Geophys. Res. Lett.*, 43, doi: 10.1002/2016GL071899, 2016.

809 Keeling, C. D., Whorf, T. P., Wahlen, M., and van der plicht, J.: Interannual extremes in the rate
810 of rise of atmospheric carbon dioxide since 1980, *Nature*, 375, 666 – 670, 1995.

811 Key, R. M., et al,: A global ocean carbon climatology: Results from Global Data Analysis
812 Project (GLODAP), *Global Biogeochem. Cycles*, 18, GB4031, doi:10.1029/2004GB002247,
813 2004

814 Krey, J., Bahenerd, B.: *Phytoplankton production atlas of the international Indian Ocean*
815 *expedition*, Institut fur Meereskundeander Universitat Kiel, Kiel, German, 1976.

816 Large, W. G., McWilliams, J. C., Doney, S. C.: Oceanic vertical mixing: A review and a model
817 with a nonlocal boundary layer parameterization, *Rev. Geophys.*, 32, 363 – 403, doi:
818 10.1029/94RG01872, 1994.

819 Laws, E. A., P. G. Falkowski, W.O. Smith, Jr., H. Ducklow and J. J. McCarthy: Temperature
820 effects on export production in the open ocean, *Global Biogeochem. Cycles*, 14, 1231 – 1246,
821 2000.

822 Le Quere, C., Orr, J. C., Monfray, P., Aumont, O.: Interannual variability of the oceanic sink of
823 CO₂ from 1979 through 1997, *Global Biogeochem. Cycles.*, 14, p1247 – 1265, doi:
824 10.1029/1999GB900049, 2000.

825 Lee, P. F., Chen, I. C., Tzeng, W. N.: Spatial and Temporal distributions patterns of bigeye tuna
826 (*Thunnusobsesus*) in the Indian Ocean, *Zoological studies-Taipei-*, 44(2), 260, 2005.

827 Lehodey .P., Senina I., Sibert. J., Bopp. L., Calmettes B., Hampton .J., Murtugudde. R.:
828 Preliminary forecasts of Pacific bigeye tuna population trends under the A2 IPCC scenario, *Prog*
829 *in Oceanography.*, 86, 302 – 315, doi:10.1016/j.pocean.2010.04.021, 2010.

830 Liao, X., Zhan, H., Du, Y.: Potential new production in two upwelling regions of the Western
831 Arabian Sea: Estimation and comparison, *J. Geophys. Res. Oceans.*, 121,
832 doi:10.1002/2016JC011707, 2016.

833 Lopez-Urrutia, A., E. San Martin, R. P. Harris, and X. Irigoien.: Scaling the metabolic balance of
834 the oceans, *Proc. Natl. Acad. Sci. U.S.A.*, 103, 8739-8744,doi:10.1073/pnas.0601137103, 2006.

835 Louanchi. F., N. Metzl., and Alain Poisson.: Modelling the monthly sea surface f_{CO2} fields in the
836 Indian Ocean, *Marine Chemistry*, 55, 265 – 279, 1996.

837 Marra, J. F., Veronica P. Lance, Robert D. Vaillancourt, Bruce R. Hargreaves.: Resolving the
838 ocean’s euphotic zone, *Deep Sea. Res. pt. I.*, 83, 45 -50, doi:10.1016/j.dsr.2013.09.005, 2014.

839 Matsumoto K., Tokos. K. S., Price., A. R., Cox. S. J.: First description of the Minnesota Earth
840 System Model for Ocean biogeochemistry (MESMO 1.0), *Geosci. Model Dev.*, 1, 1-15,
841 doi:10.5194/gmd-1-1-2008, 2008.

842 McCreary, J., Murtugude, R., Vialard, J., Vinayachandran, P., Wiggert, J. D., Hood, R. R.,
843 Shankar, D., Shetye, S.: Biophysical processes in the Indian Ocean, *Indian Ocean*
844 *Biogeochemical Processes and Ecological Variability.*, 9 – 32, doi: 10.1029/GM185, 2009.

845 Mehrbach, C., C. H. Culberson, J. E. Hawley, and R. M. Pytkowicz.: Measurement of the
846 apparent dissociation constants of carbonic acid in seawater at atmospheric pressure, *Limnol.*
847 *Oceanogr.*, 18, 897 – 907, 1973.

848 Moisan, J. R., Moisan, A. T., Abbott, M. R.: Modelling the effect of temperature on the
849 maximum growth rates of phytoplankton populations, *Eco. Modelling.*, 153, 197-215,
850 doi:10.1016/S0304-3800(02)00008, 2002.

851 Morel, A.: Optical modeling of the upper ocean in relation to its biogenous matter content (Case
852 1 Waters), *J. Geophys. Res.*, 93, 10479-10, 768, doi: 10.1029/JC093iC09p10749, 1988.

853 Murtugudde R., McCreary J. P., Busalacchi, A. J.: Oceanic processes associated with anomalous
854 events in the Indian Ocean with relevance to 1997-1998, *J. Geophys. Res.*, 105, 3295-3306, doi:
855 10.1029/1999JC900294, 2000.

856 Murtugudde, R. G., S. R. Signorini, J. R. Christian, A. J. Busalacchi, C. R. McClain, and J.
857 Picaut.: Ocean color variability of the tropical Indo-Pacific basin observed by SeaWiFS during
858 1997 – 1998, *J. Geophys. Res.*, 104(C8), 18351 – 18366, doi.10.1029/1999JC900135, 1999a.

859 Murtugudde, R., Busalacchi, A. J.: Interannual variability of the dynamics and thermodynamics
860 of the tropical Indian Ocean, *J. Clim.* 12, 2300-2326, doi:10.1175/1520-0442, 1999b.

861 Murtugudde, R., Seager, R., Thoppil, P.: Arabian Sea response to monsoon variations,
862 *Paleoceanography.*, 22, PA4217, doi:10.1029/2007PA001467, 2007.

863 Najjar, R. G., Keeling, R. F.: Analysis of the mean annual cycle of the dissolved oxygen
864 anomaly in the world ocean, *J. Mar. Res.*, 55, 117 – 151, doi:10.1357/0022240973224481, 1997.

865 Najjar, R. G., Orr, J. C.: Design of OCMIP-2 simulations of chlorofluorocarbons, the solubility
866 pump and common biogeochemistry, <http://www.ipsl.jussieu.fr/OCMIP/>, 1998.

867 Najjar, R. G., Sarmiento, J. L., Toggweiler, J. R.: Downward transport and fate of organic matter
868 in the ocean: simulations with a general circulation model, *Global Biogeochem. Cycles.*, 6, 45-
869 76, doi/10.1029/91GB02718, 1992.

870 Naqvi, S. W. A., Moffett, J. W., Gauns, M. U., Narvekar, P. V., Pratihary, A. K., Naik, H.,
871 Shenoy, D. M., Jayakumar, D. A., Goepfert, T. J., Patra, P. K., Al-Azri, A., and Ahmed, S. I.:
872 The Arabian Sea as a high-nutrient, low-chlorophyll region during the late Southwest Monsoon,
873 *Biogeosciences.*, 7, 2091-2100, doi:10.5194/bg-7-2091-2010, 2010.

874 Naqvi, S., Naik, H., Narvekar, P.: The Arabian Sea, in *Biogeochemistry*, edited by K. Black and
875 G. Shimmield, pp. 156 – 206, Blackwell, Oxford, 2003.

876 Orr, J. C., and co-authors.: Anthropogenic ocean acidification over the twenty-first century and
877 its impact on calcifying organisms, *Nature*, 437, 681 – 686, doi:10.1038/nature04095, 2005.

878 Orr, J. C., and co-authors.: Estimates of anthropogenic carbon uptake from four three-
879 dimensional global ocean models, *Glob. Biogeochem. Cycles.*, 15, p43 – 60, doi:
880 10.1029/2000GB001273, 2001.

881 Orr, J. C., Aumont, O., Bopp, L., Calderia, K., Taylor, K., et. al.: Evaluation of seasonal air-sea
882 CO₂ fluxes in the global carbon cycle models, International open Science conference (Paris, 7-
883 10 Jan. 2003), 2003.

884 Osawa, T., Julimantoro, S.: Study of fishery ground around Indonesia archipelago using remote
885 sensing data, *International archives of the Photogrammetry, Remote sensing and spatial*
886 *information science.*, vol XXXVIII, part-8, 2010.

887 Parsons, T. R., Takahashi, M., Habgrave, B.: In *Biological Oceanographic Processes*, 3rd ed.,
888 330pp., Pergamon Press, New York, doi: 10.1002/iroh.19890740411, 1984.

889 Prasanna Kumar, .S., Muraleedharan, P. M., Prasad, T. G., Gauns, M., Ramaiah, N., de Souza, S.
890 N., Sardesai, S., Madhupratap, M.: Why is the Bay of Bengal less productive during summer
891 monsoon compared to the Arabian Sea?, *Geophys. Res. Lett.*, 29(24), 2235,
892 doi:10.1029/2002GL016013, 2002.

893 Prasanna Kumar, S., Roshin, P. R., Narvekar, J., Dinesh Kumar, P., Vivekanandan, E.: What
894 drives the increased phytoplankton biomass in the Arabian Sea?, *Current Science*, 99(I), 101 –
895 106, 2010.

896 Prassana Kumar. S, Ramaiah. N, Gauns. M., Sarma V. V. S. S., Muraleedharan. P. M.,
897 RaghuKumar. S., Dileep Kumar., Madhupratap. M.: Physical forcing of biological productivity
898 in the Northern Arabian Sea during the Northeast Monsoon, *Deep Sea Res. Pt. II.*, 48, 1115-
899 1126, doi:10.1016/S0967-0645(00)00133-8, 2001.

900 Praveen, V., Ajayamohan, R. S., Valsala, V., Sandeep, S.: Intensification of upwelling along
901 Oman coast in a warming scenario, *Geophys. Res. Lett.*, 43, doi:10.1002/2016GL069638, 2016.

902 Press, W. H., and others: *Numerical Recipes in FORTRAN*. Cambridge University Press,
903 Cambridge, England, 1996.

904 Qasim, S. Z.: Biological productivity of the Indian Ocean, *J. Mar. Sci.*, 6, 122 – 137, 1977.

905 Qasim, S. Z.: Oceanography of Northern Arabian Sea, *Deep Sea Res.*, 29(9A), 1041 – 1068,
906 doi:10.1016/0198-0149(82)90027-9, 1982.

907 Redi, M.: Oceanic isopycnal mixing by coordinate rotation, *J. Phys. Oceanogr.*, 12, 1154 – 1158,
908 doi: 10.1175/1520-0485, 1982.

909 Regaudie-de-Gioux, A., and C. M. Duarte.: Compensation irradiance for planktonic community
910 metabolism in the ocean, *Global Biogeochem. Cycles*, 24, GB4013,
911 doi:10.1029/2009GB003639, 2010.

912 Roxy, M. K., Modi, A., Murtugudde, R., Valsala, V., Panickal, S., Prasanna Kumar, S.,
913 Ravichandran, M., Vichi, M., Levy, M.: A reduction in marine primary productivity driven by
914 rapid warming over the tropical Indian Ocean, 43, 826 – 833, *J. Geophys. Res. Letters.*,
915 doi:10.1002/2015GL066979, 2015.

916 Ryther, J., Menzel, D.: On the production, composition, and distribution of organic matter in the
917 Western Arabian Sea, *Deep Sea Research and Oceanographic Abstracts.*, 12(2), 199 -209.
918 doi:10.1016/0011-7471(65)90025-2, 1965.

919 Ryther, J.: Photosynthesis in the ocean as function of light Intensity, *Limnol. Oceanogr.*, vol 1,
920 issue 1, doi: 10.4319/lo.1956.1.1.0061, 1956.

921 Sarma V. V. S. S.: Net plankton community production in the Arabian Sea based on O₂ mass
922 balance model, *Glob. Biogeochem. Cycles.*, 18, GB4001, doi:10.1029/2003GB002198, 2004.

923 Sarma, V. V. S. S.: An evaluation of physical and biogeochemical processes regulating the
924 perennial suboxic conditions in the water column of the Arabian Sea, *Global Biogeochem.*
925 *Cycles.*, 16, doi:10.1029/2001GB001461, 2002.

926 Sarmiento, J. L., and Gruber, N.: Ocean Biogeochemical Dynamics, Princeton University Press,
927 New Jersey, 2006.

928 Sarmiento, J. L., Monfray, P., Maier-Reimer., Aumont, O., Murnane, R. J., Orr, J. C.: Sea-air
929 CO₂ fluxes and carbon transport: A comparison of three ocean general circulation models,
930 Global Biogeochem. Cycles., 14, p1267 – 1281. doi: 10.1029/1999GB900062, 2000.

931 Schott, F.: Monsoon response of the Somali current and associated upwelling, Prog.Oceanogr.,
932 12, 357 – 381, doi:10.1016/0079-6611(83)90014-9, 1983.

933 Smetacek, V., and Passow, U.: Spring bloom initiation and Sverdrup's critical depth model,
934 Limnol. Oceanogr., 35, 228 – 234, doi: 10.4319/lo.1990.35.1.0228, 1990.

935 Smith, L. S.: Understanding the Arabian Sea: Reflections on the 1994-1996 Arabian Sea
936 Expedition, Deep Sea Res. Pt. II., 48, 1385-1402, doi:10.1016/S0967-0645(00)00144-2, 2001.

937 Smith, R. L., Bottero, L. S.: On upwelling in the Arabian Sea. In Angel, M (ed) A voyage of
938 Discovery. Pergamon Press, New York, p. 291 – 304, 1977.

939 Smith, S. L., Codispoti, L. A.: Southwest monsoon of 1979: chemical and biological response of
940 Somali coastal waters. Science, 209, 597 – 600. doi:10.1126/science.209.4456.597, 1980.

941 Smith, S. L.: Biological indications of active upwelling in the northwestern Indian Ocean in 1964
942 and 1979, a comparison with Peru and northwest Africa, Deep Sea Res., 31, 951 – 967,
943 doi:10.1016/0198-0149(84)90050-5, 1984.

944 Susanto. R., Gordon, A. L., Zheng. Q.: Upwelling along the coasts of Java and Sumatra and its
945 relation to ENSO, J. Geophys. Res. Lett., 28, 1599-1602, doi: 10.1029/2000GL011844, 2001.

946 Swallow, J. C.: Some aspects of the physical oceanography of the Indian Ocean, *Deep Sea Res.*,
947 31, 639 – 650, doi:10.1016/0198-0149(84)90032-3, 1984.

948 Takahashi, T., Sutherland, S. C., Wanninkhof, R., Sweeney, C., Feely, R. A., Chipman, D. W.,
949 Hales, B., Friederich, G., Chavez, F., Sabine, C., et al.: Climatological mean and decadal
950 changes in surface ocean pCO₂ and net sea-air CO₂ flux over the global oceans. *Deep Sea Res.*,
951 Pt. II., 56, 554 – 557, doi:10.1016/j.dsr2.2008.12.009, 2009.

952 Valsala V., Maksyutov, S.: A short surface pathway of the subsurface Indonesian Throughflow
953 water from the Java Coast associated with upwelling, Ekman Transport, and Subduction. *Int. J.*
954 *Oceanogr.*, 15, doi: 10.1155/2010/540743, 2010a.

955 Valsala V., Maksyutov, S.: Interannual variability of air-sea CO₂ flux in the north Indian Ocean,
956 *Ocean Dynamics.*, 1 – 14, doi 10.1007/s10236-012-0588-7, 2013.

957 Valsala V., R. R. Rao.: Coastal Kelvin waves and dynamics of gulf of Aden eddies, *Deep Sea*
958 *Res.*, Pt. I., 116, 174 – 186, <https://doi.org/10.1016/j.dsr.2016.08.003>, 2016.

959 Valsala, K. V., Maksyutov, S., Ikeda, M.: Design and Validation of an offline oceanic tracer
960 transport model for a carbon cycle study, *J. clim.*, 21, doi: 10.1175/2007JCLI2018.1, 2008.

961 Valsala, V., Maksyutov, S., Murtugudde, R.: Interannual to Interdecadal Variabilities of the
962 Indonesian Throughflow Source Water Pathways in the Pacific Ocean, *J. Phys. Oceanogr.*, 41,
963 1921–1940, doi: 10.1175/2011JPO4561.1, 2011.

964 Valsala, V., Maksyutov, S.: Simulation and assimilation of global ocean pCO₂ and air-sea CO₂
965 fluxes using ship observations of surface ocean pCO₂ in a simplified biogeochemical model,
966 *Tellus.*, 62B, doi: 10.1111/j.1600-0889.2010.00495, 2010b.

967 Valsala, V., Murtugudde, R.: Mesoscale and Intraseasonal Air-Sea CO₂ Exchanges in the
968 Western Arabian Sea during Boreal Summer, *Deep Sea Res. Pt. I*, 103, 103-113,
969 doi:10.1016/j.dsr.2015.06.001, 2015.

970 Valsala, V., Roxy, M., Ashok, K., Murtugudde, R.: Spatio-temporal characteristics of seasonal to
971 multidecadal variability of pCO₂ and air-sea CO₂ fluxes in the equatorial Pacific Ocean, *J.*
972 *Geophys. Res.*, 119, 8987 – 9012, doi:10.1002/2014JC010212, 2014.

973 Valsala, V.: Different spreading of Somali and Arabian coastal upwelled waters in the northern
974 Indian Ocean: A case study. *J. Phy. Oceanogr.*, 803 – 816, doi: [https://doi.org/10.1007/s10872-](https://doi.org/10.1007/s10872-009-0067-z)
975 [009-0067-z](https://doi.org/10.1007/s10872-009-0067-z), 2009.

976 Vialard, J. and co-authors.: Air-Sea Interactions in the Seychelles-Chagos Thermocline Ridge
977 Region, *BAMS*, doi:10.1175/2008BAMS2499.1, 2009.

978 Vinayachandran P. N., Yamagata, T.: Monsoon Response of the Sea around Sri Lanka:
979 Generation of Thermal Domes and Anticyclonic Vortices, *J. Phy. Oceano.*, 28, 1946 – 1960, doi:
980 10.1175/1520-0485, 1998.

981 Vinayachandran, P. N., Chauhan, P., Mohan, M., Nayak, S.: Biological response of the sea
982 around Sri Lanka to summer monsoon, *Geophys. Res. Lett.*, 31, L01302,
983 doi:10.1029/2003GL018533, 2004.

984 Wang .X. J., Behrenfeld. M., Le Borgne .R., Murtugudde .R., and Boss. E.: Regulation of
985 phytoplankton carbon to chlorophyll ratio by light, nutrients and temperature in the equatorial
986 Pacific Ocean: a basin-scale model. *Biogeosciences.*, 6, 391 – 404, doi:10.5194/bg-6-391-2009,
987 2009.

988 Weiss, R. F.: Carbon dioxide in water and seawater: The solubility of a non-ideal gas, *Mar.*
989 *Chem.*, 2, 203-215, 1974.

990 Wiggert J. D., Jones. B. H., Dickey .T D., Brink .K. H., Weller .R .A., Marra. J., Codispoti. L.
991 A.: The Northeast Monsoon's impact on mixing, phytoplankton biomass and nutrient cycling in
992 the Arabian Sea, *Deep Sea Res. Pt. II*, 47, 1353-1385, doi:10.1016/S0967-0645(99)00147-2,
993 2000.

994 Wiggert, J. D., Hood, R. R., Banse, K., Kindle, J. C.: Monsoon-driven biogeochemical processes
995 in the Arabian Sea, *Progr. Oceanogr.*, 65, 176-213, doi:10.1016/j.pocean.2005.03.008, 2005.

996 Wiggert. J. D., Murtugudde, R. G., Christian J. R.: Annual ecosystem variability in the tropical
997 Indian Ocean: results of a coupled bio-physical ocean general circulation model, *Deep Sea Res.*
998 *Pt. II.*, 53, 644-676, doi:10.1016/j.dsr2.2006.01.027, 2006.

999 Xie, S. P., Annamalai, H., Schott, F. A., McCreary Jr. J. P.: Structure and mechanism of south
1000 Indian ocean climate variability, *J. clim.*, 15, 864 – 878, doi: 10.1175/1520-0442, 2002.

1001 Xing W., Xiaomei. L., Haigang Z., Hailong. L.: Estimates of potential new production in the
1002 Java-Sumatra upwelling system, *Chinese Journal of Oceanology and Limnology.*, 30, 1063-
1003 1067, doi:10.1007/s00343-012-1281, 2012.

1004 Yamanaka, Y., Yoshie, N, Masahiko Fujii, Maka .N. Aita and Kishi. M. J.: An Ecosystem
1005 coupled with Nitrogen-Silicon-Carbon cycles applied to station A7 in the Northwestern Pacific,
1006 *J. of Oceanogr.*, 60, p227-241, doi: 10.1023/B:JOCE.0000038329.91976.7d, 2004.

1007 Zhou X., Weng. E., Luo., Y.: Modelling patterns of nonlinearity in the ecosystem responses to
1008 temperature, CO₂ and precipitation changes, *Eco. Appli.*, 18, 453 – 466, doi: 10.1890/07-0626.1,
1009 2008.

1010

Table: 1 WAS = Western Arabian Sea, SLD = Sri Lanka Dome, SC = Sumatra Coast, SCTR = Seychelles-Chagos Thermocline Ridge. JJAS mean and the climatological annual mean of CO₂ flux from Takahashi observations, constZc, and varZc simulations. Units are mol m⁻² yr⁻¹.

Regions	CO ₂ flux (mol m ⁻² yr ⁻¹)					
	JJAS Mean			Annual Mean		
	OBS	constZc	varZc	OBS	constZc	varZc
WAS	1.99	1.44 ± 0.2	2.31 ± 0.4	0.94	0.80 ± 0.1	1.07 ± 0.2
SLD	1.79	-0.008 ± 0.2	0.24 ± 0.09	0.8	-0.02 ± 0.1	0.10 ± 0.2
SC	0.31	0.60 ± 0.5	1.51 ± 1.01	0.21	0.21 ± 0.3	0.53 ± 0.5
SCTR	0.82	-0.32 ± 0.3	-0.05 ± 0.4	0.55	-0.02 ± 0.1	-0.07 ± 0.2

Table: 2 Same as Table 1, but for pCO₂. Units are µatm.

Regions	pCO ₂ (µatm)					
	JJAS Mean			Annual Mean		
	OBS	constZc	varZc	OBS	constZc	varZc
WAS	397.58	389.18 ± 3.7	399.95 ± 5.01	394.69	389.62 ± 3.9	391.19 ± 4.7
SLD	382.44	371.67 ± 6.04	379.24 ± 8.9	380.21	370.76 ± 6.1	374.94 ± 9.6
SC	372.52	382.36 ± 12.7	402.14 ± 21.8	372.69	374.65 ± 9.3	381.76 ± 13.6
SCTR	377.18	365.71 ± 5.08	370.72 ± 7.4	379.89	372.69 ± 4.7	369.00 ± 5.4

Table: 3 JJAS mean and the climatological annual mean of export production from satellite-derived Net Primary Production data, constZc, and varZc simulations. Units are $\text{g C m}^{-2} \text{yr}^{-1}$.

Regions	Export Production ($\text{g C m}^{-2} \text{yr}^{-1}$)					
	JJAS Mean			Annual Mean		
	OBS	constZc	varZc	OBS	constZc	varZc
WAS	123.57	84.81 ± 16.04	147.19 ± 23.8	94.31	77.41 ± 15.1	122.54 ± 25.2
SLD	51.54	167.71 ± 59.04	151.51 ± 46.4	43.25	144.43 ± 49.8	156.08 ± 43.8
SC	58.87	260.11 ± 104.7	310.03 ± 99.5	54.53	172.52 ± 72.4	215.52 ± 70.8
SCTR	51.08	57.39 ± 14.2	99.23 ± 21.8	40.45	55.15 ± 17.9	80.35 ± 26.04

Table: 4 Model derived values for New production. Units are $\text{g C m}^{-2} \text{yr}^{-1}$.

Regions	New Production ($\text{g C m}^{-2} \text{yr}^{-1}$)					
	JJAS Mean			Annual Mean		
	OBS	constZc	varZc	OBS	constZc	varZc
WAS	--	150.84 ± 27.9	133.03 ± 19.5	--	108.43 ± 23.4	81.47 ± 15.7
SLD	--	141.93 ± 64.1	77.78 ± 27.6	--	111.05 ± 71.1	50.37 ± 26.3
SC	--	63.64 ± 30.9	78.11 ± 29.1	--	56.69 ± 43.3	54.58 ± 23.3
SCTR	--	12.17 ± 16.3	13.32 ± 18.6	--	13.74 ± 15.5	12.94 ± 13

Table 5: Biological pump impact over DIC in the model due to constZc and varZc simulations for JJAS and annual mean.

Regions	Biological Pump ($\text{g C m}^{-2} \text{ yr}^{-1}$)			
	constZc		varZc	
	JJAS Mean	Annual Mean	JJAS Mean	Annual Mean
WAS	45.18 ± 14.8	45.49 ± 14.38	151.7 ± 23.8	126.67 ± 24.3
SLD	89.39 ± 58.1	108.65 ± 48.6	156.07 ± 48.4	161.15 ± 43.5
SC	235.54 ± 95.4	155.21 ± 67.4	319.16 ± 94.9	222.92 ± 68.7
SCTR	30.49 ± 13.4	26.81 ± 16.8	103.13 ± 19.6	83.98 ± 23.6

Table 6: Same as Table 5, But for Solubility pump.

Regions	Solubility Pump ($\text{g C m}^{-2} \text{ yr}^{-1}$)			
	constZc		varZc	
	JJAS Mean	Annual Mean	JJAS Mean	Annual Mean
WAS	17.29 ± 3.5	9.63 ± 2.1	27.72 ± 4.8	12.92 ± 2.7
SLD	-0.09 ± 2.4	-0.32 ± 2.3	2.9 ± 3.5	1.31 ± 3.5
SC	7.22 ± 6.9	2.56 ± 3.8	18.17 ± 12.1	6.43 ± 6.0
SCTR	-3.95 ± 3.7	-0.35 ± 2.3	-0.61 ± 5.3	-0.86 ± 2.8

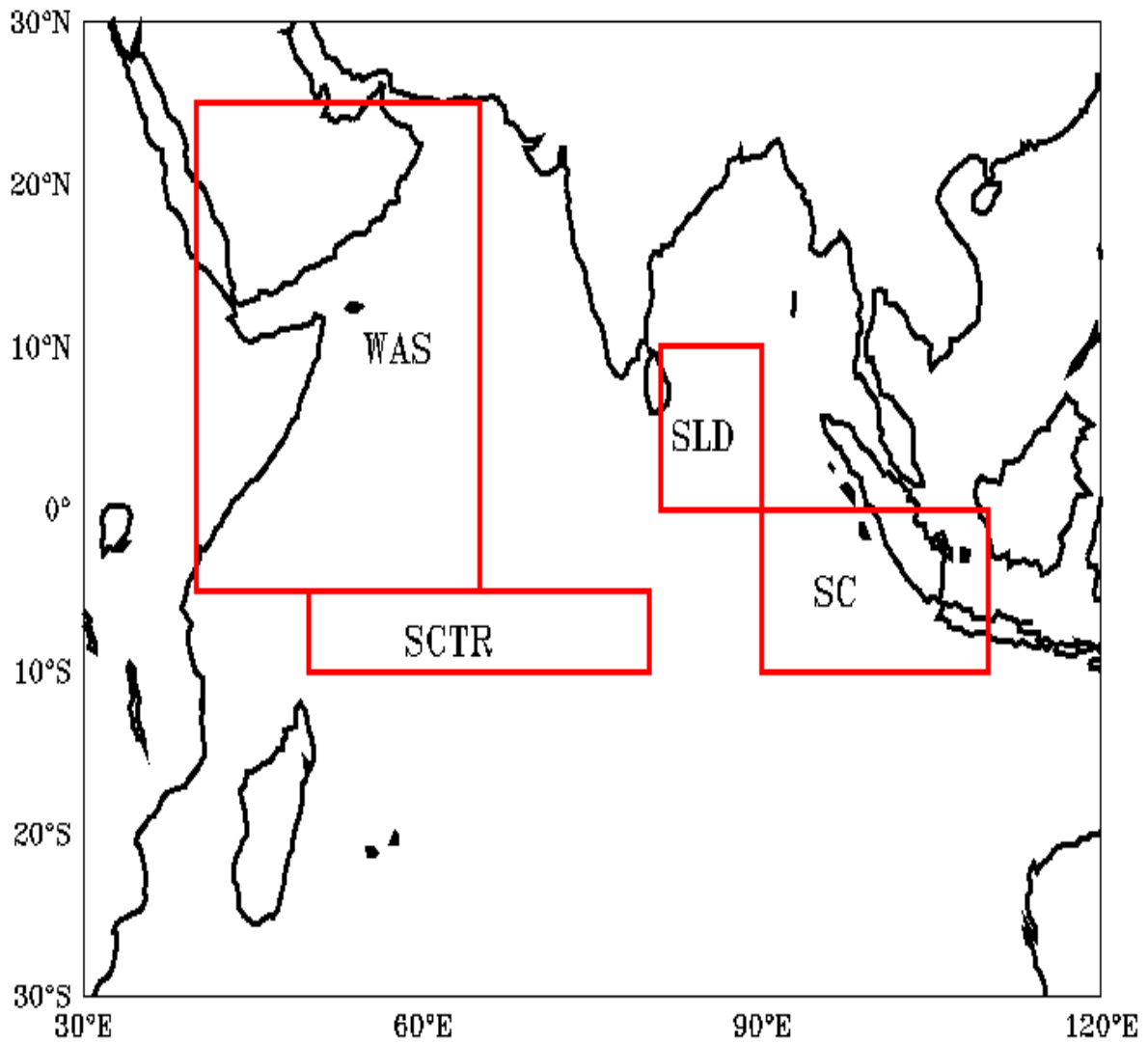


Figure 1: Red boxes shows the study regions (1) WAS (Western Arabian Sea, 40°E:65°E, 5°S:25°N) (2) SLD (Sri Lanka Dome, 81°E:90°E, 0°:10°N) (3) SCTR (Seychelles-Chagos Thermocline Ridge, 50°E:80°E, 5°S:10°S) and (4) SC (Sumatra Coast, 90°E:110°E, 0°:10°S).

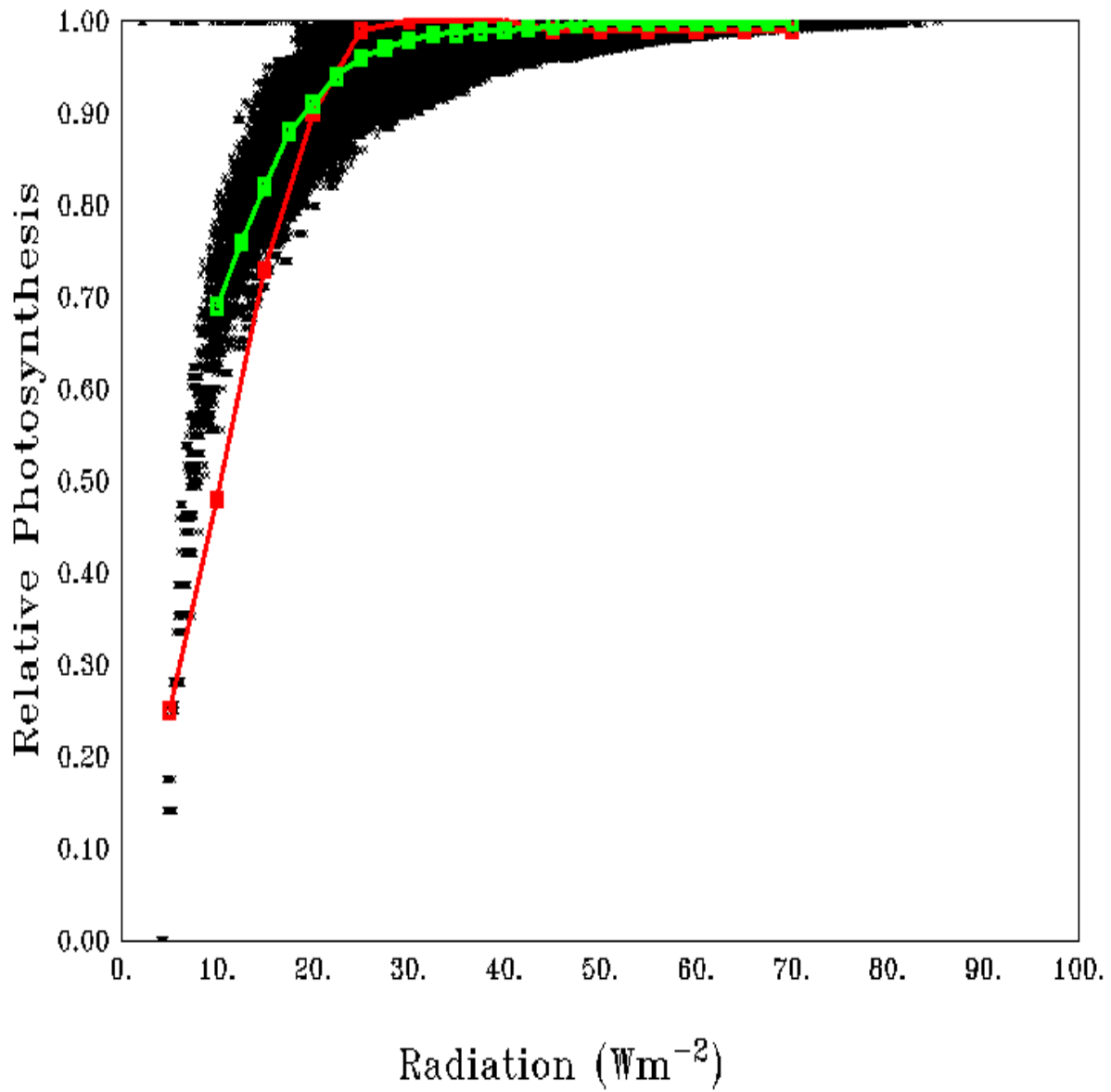


Figure 2: Scatter of average relative photosynthesis versus different light intensities in the model (black dots) and its mean (green curve). The red curve shows the theoretical P – I curve from Parsons et al., (1984).

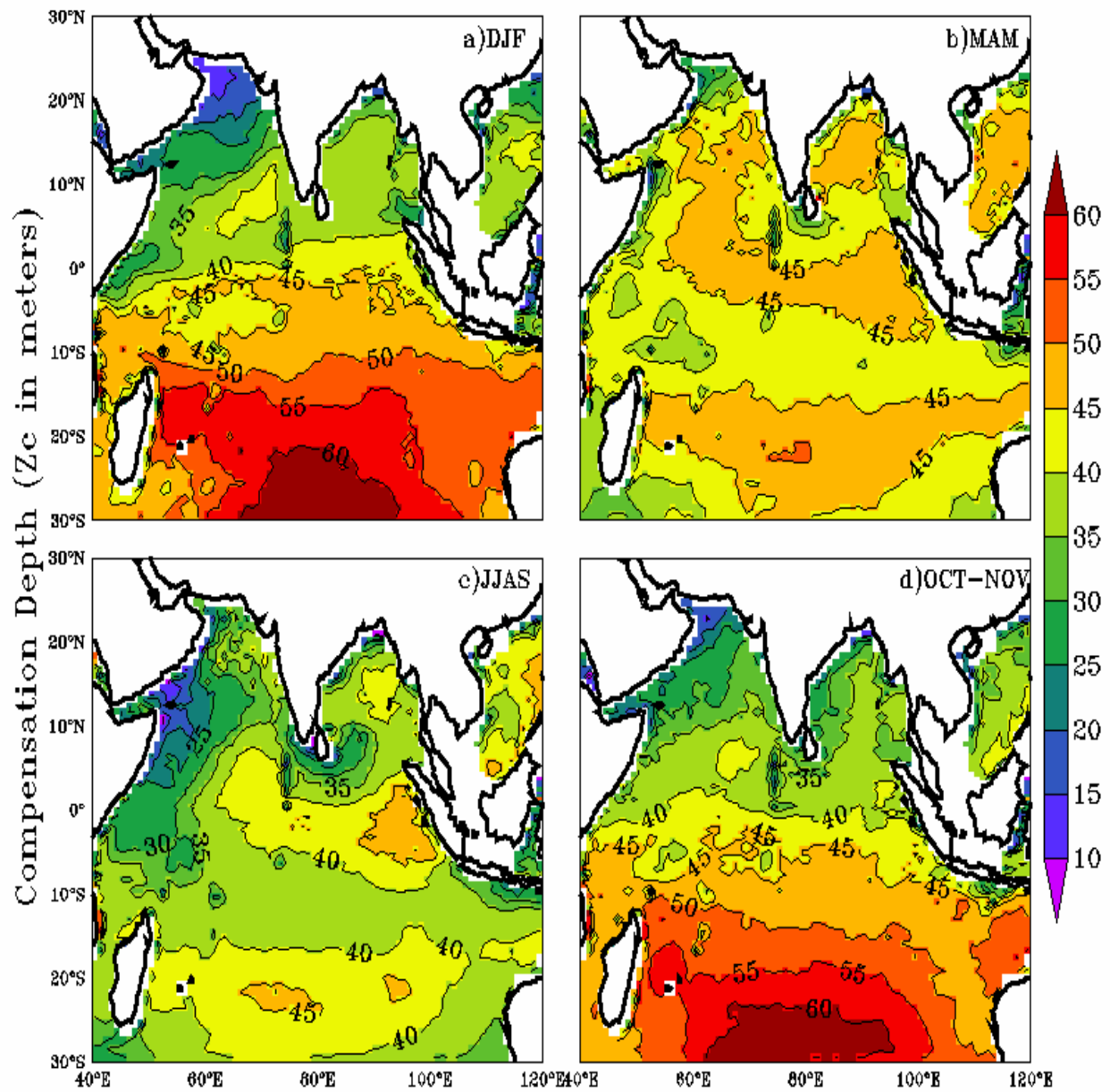


Figure 3: Seasonal-mean maps of varying compensation depth ($\text{var}Z_c$), (a) December to February (DJF), (b) March to May (MAM), (c) June to September (JJAS), (d) October to November (ON). Units are meters.

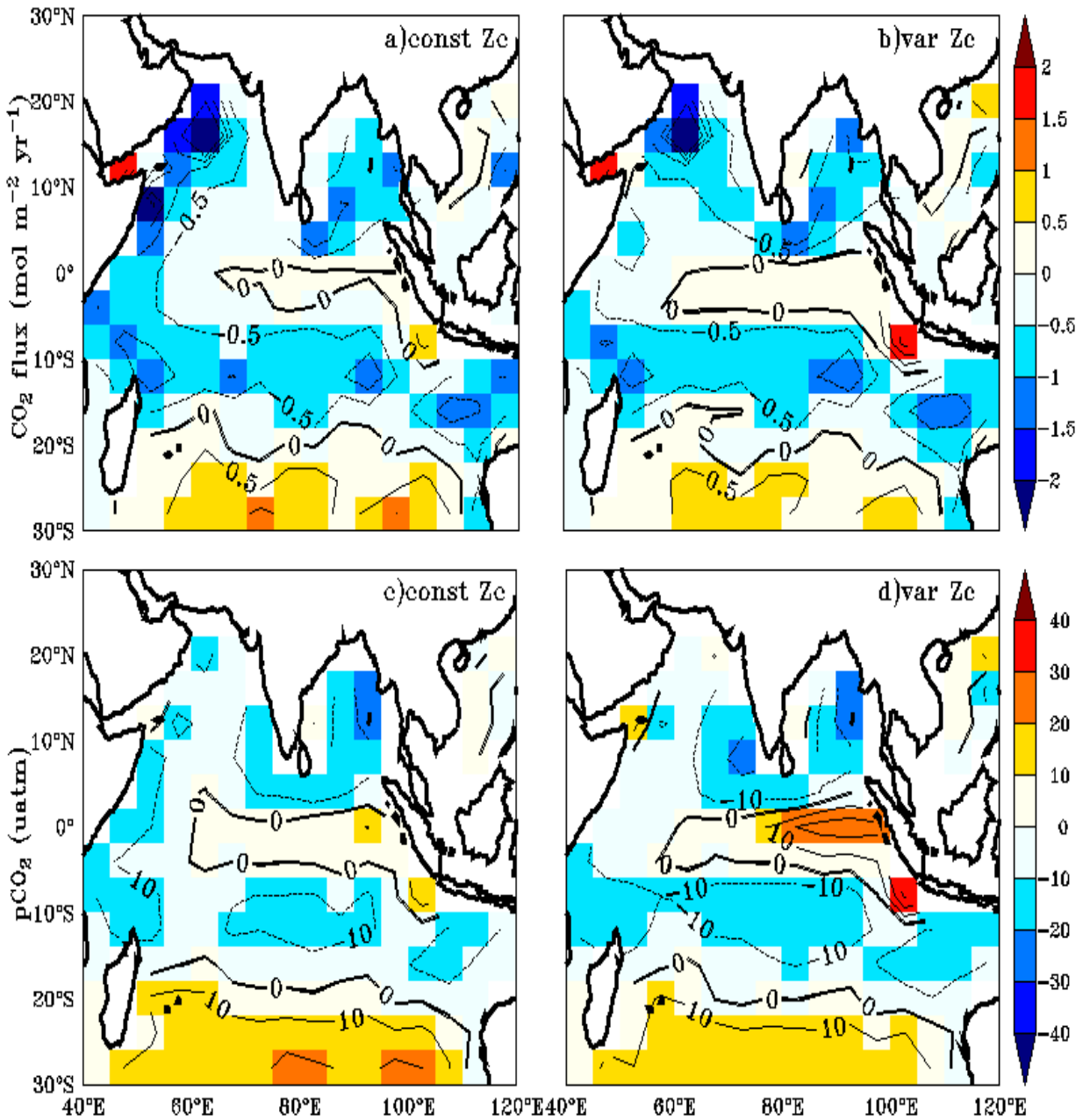


Figure 4: Annual mean biases in the model evaluated against Takahashi et al. (2009) observations for CO₂ flux (a, b) and pCO₂ (c, d) with constant Z_c (constZ_c) and varying Z_c (varZ_c). Units of CO₂ flux and pCO₂ are mol m⁻² yr⁻¹ and μatm, respectively.

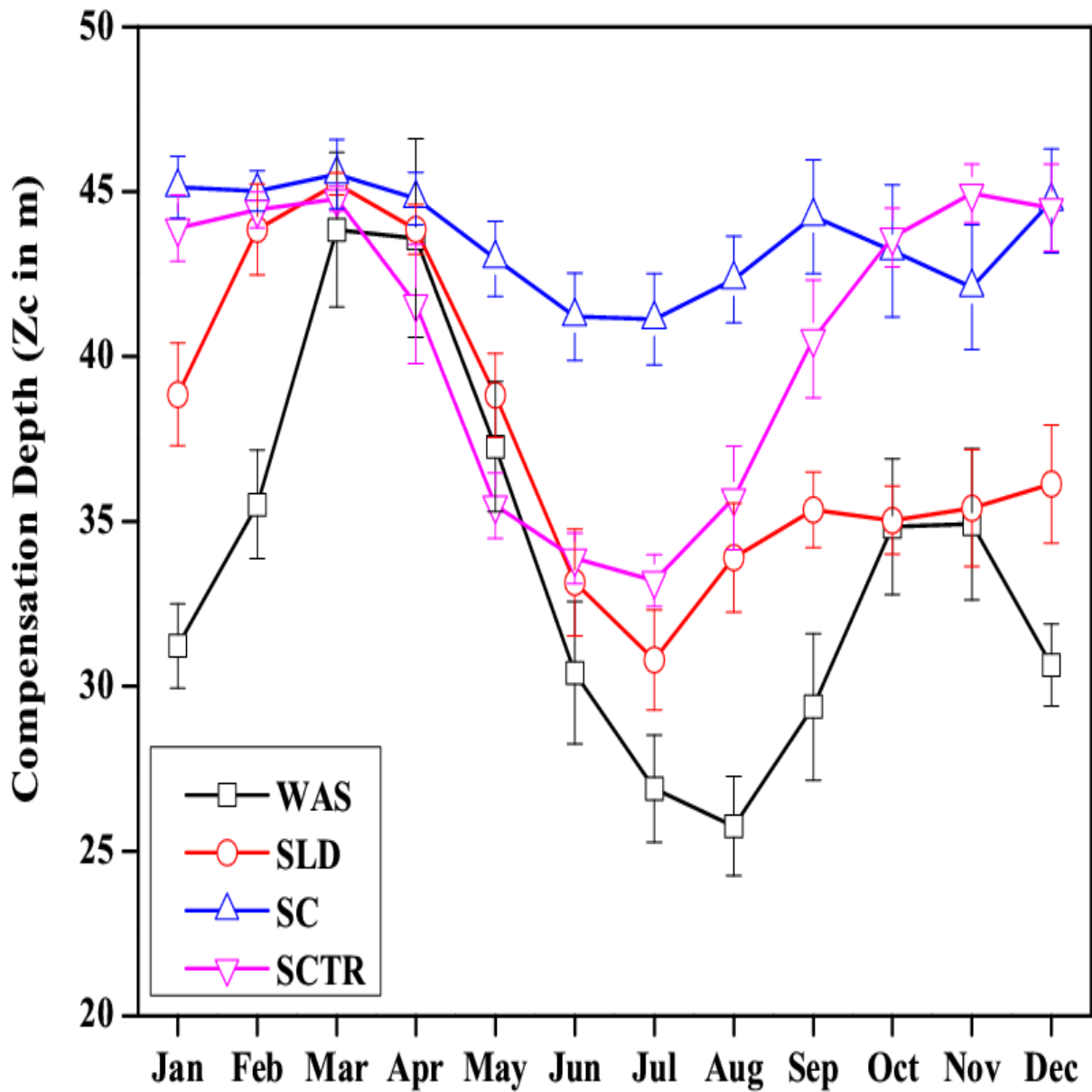


Figure 5: Seasonal variations in varZc over the study regions shown as climatology computed over 1990-2010. Error bar shows standard deviations of individual months over these years. Units are meters.

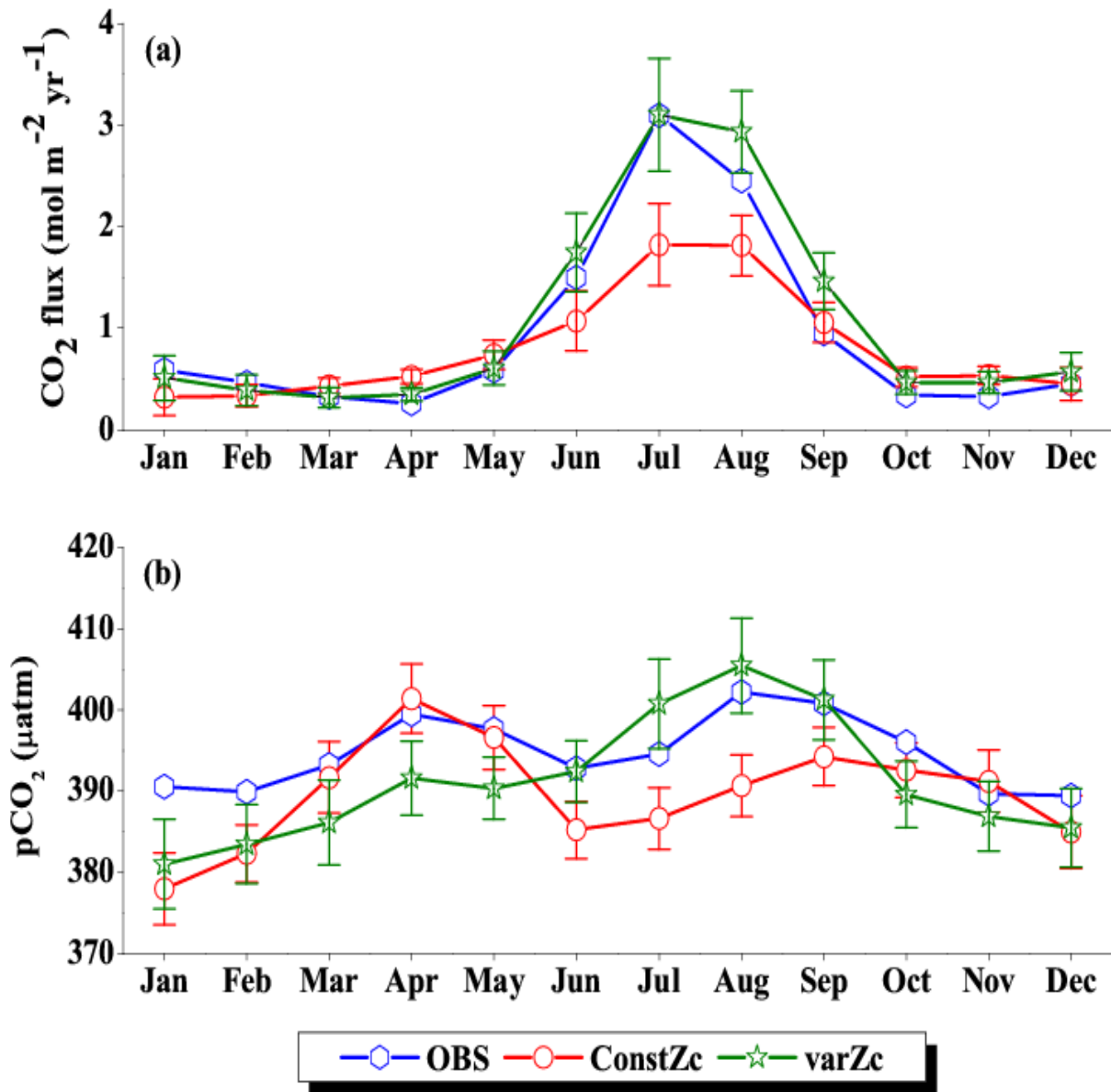


Figure 6: Comparison of model (a) CO₂ flux and (b) pCO₂ simulated with constZc and varZc with that of Takahashi et al. (2009) observations (OBS) over WAS as climatology computed over 1990-2010. Error bar shows standard deviations of individual months over these years. Units of CO₂ flux and pCO₂ are mol m⁻² yr⁻¹ and µatm, respectively. Legend is common for both graphs.

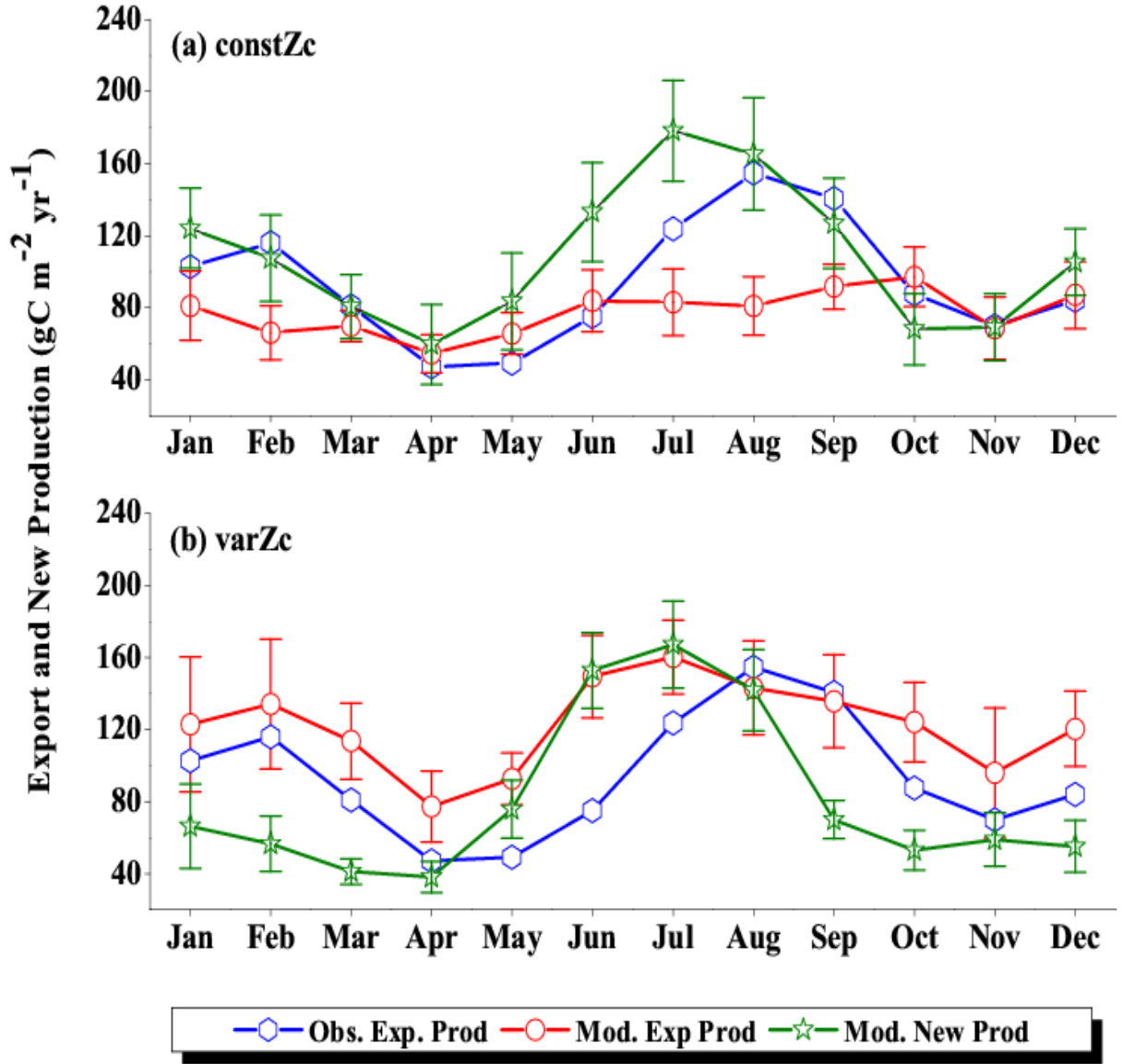


Figure 7: Comparison of model export production (Mod. Exp. Prod) and new production (Mod. New Prod) with satellite-derived export production (Obs. Exp. Prod) for (a) ConstZc and (b) varZc simulations for WAS. Units are $\text{g C m}^{-2} \text{ yr}^{-1}$. Legends are common for both graphs.

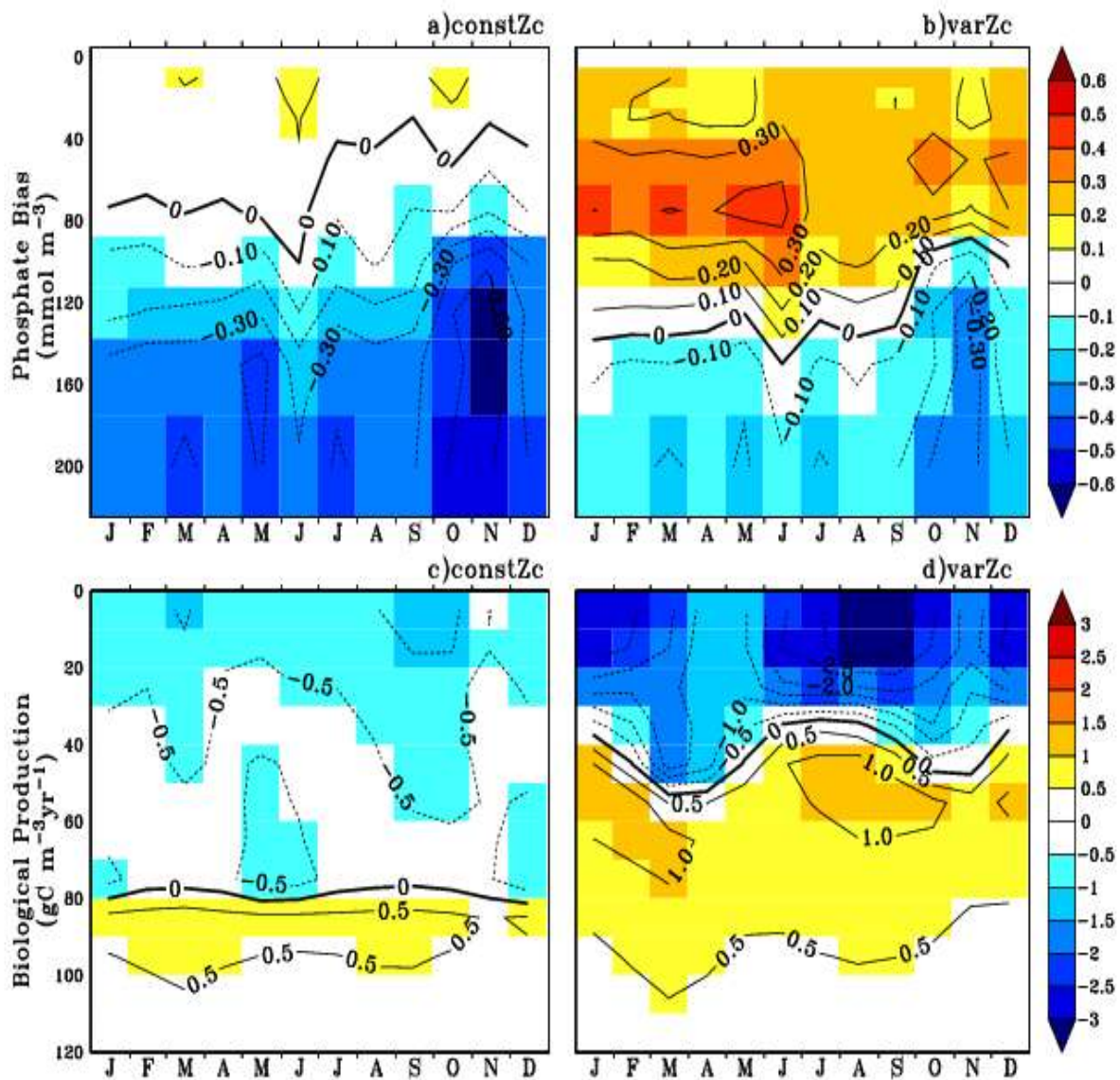


Figure 8: Annual mean bias of model phosphate when compared with climatological observational data (a) for constZc and (b) for varZc simulations. Corresponding annual mean biological source/sink profiles (c, d) in the model for WAS. Unit of phosphate is mmol m^{-3} and biological source/sink is $\text{g C m}^{-3} \text{yr}^{-1}$.

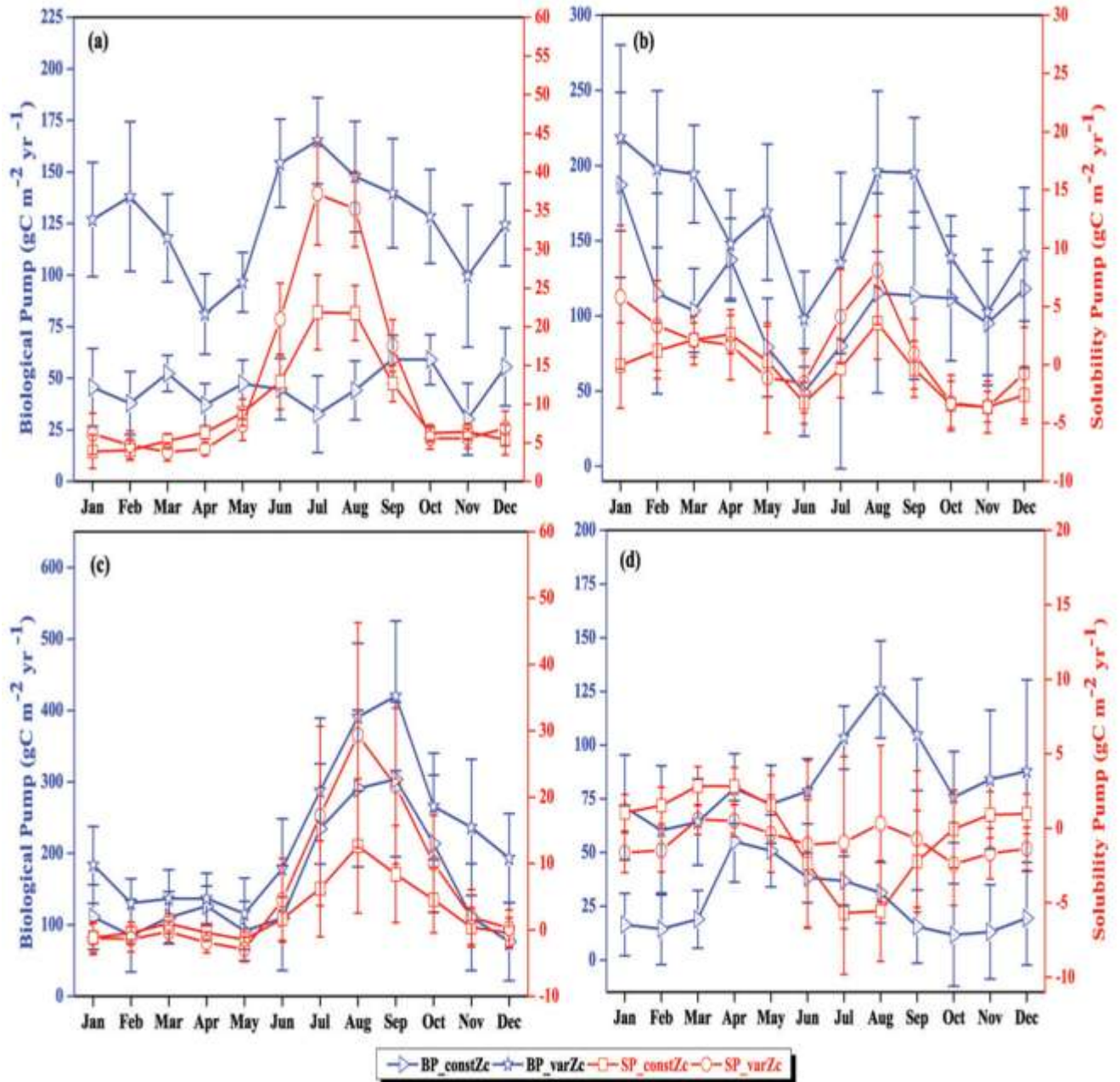


Figure 9: The strength of the biological pump (BP, black lines) and solubility pump (SP, red lines) from constZc and varZc simulations for (a) WAS (b) SLD (c) SC and (d) SCTR. The left axis shows the biological pump and the right axis shows the solubility pump. Error bar shows standard deviations of individual months over the years 1990 - 2010. Units are $\text{g C m}^{-2} \text{ yr}^{-1}$.

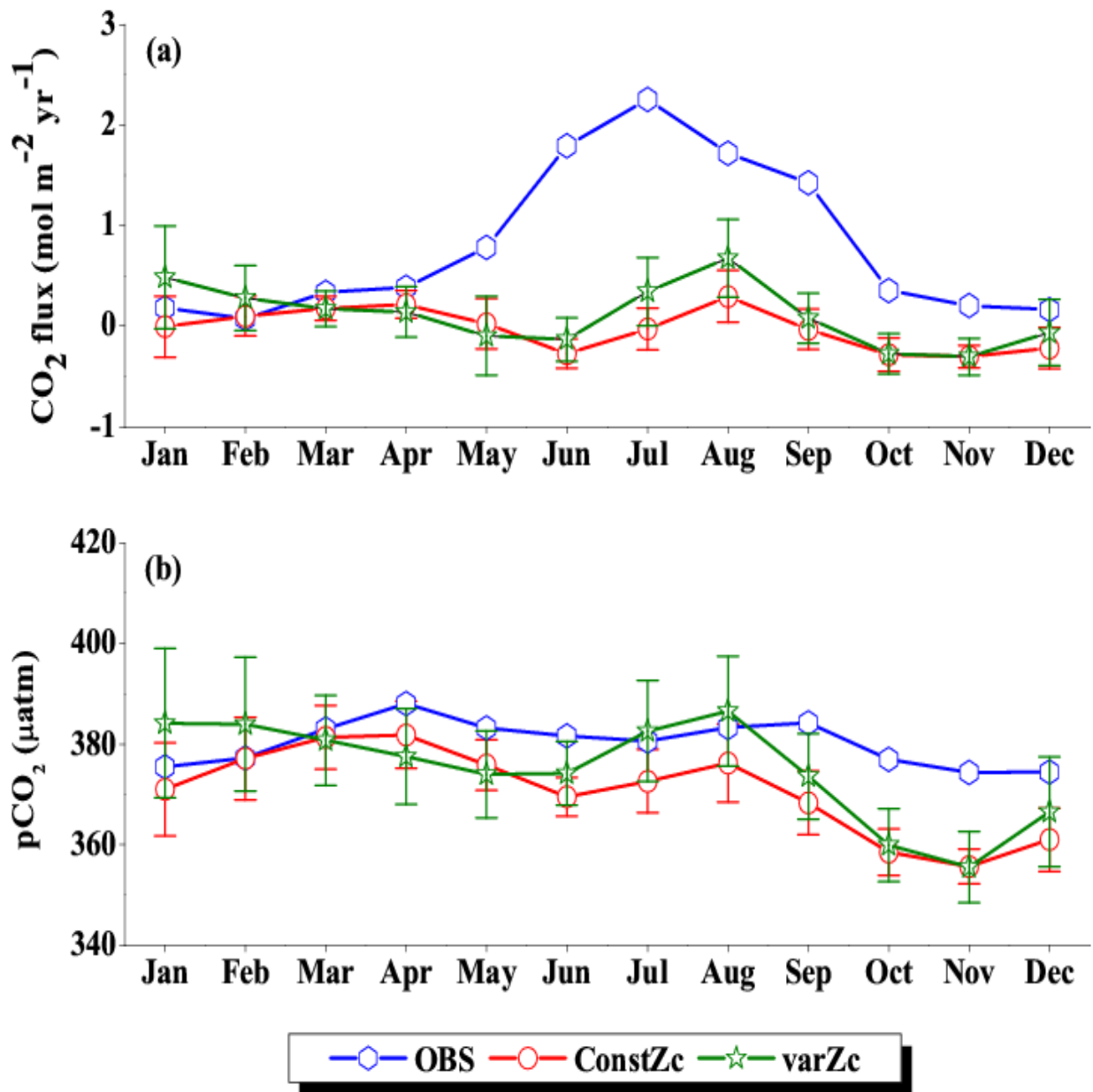


Figure 10: Same as Figure (6), but for SLD.

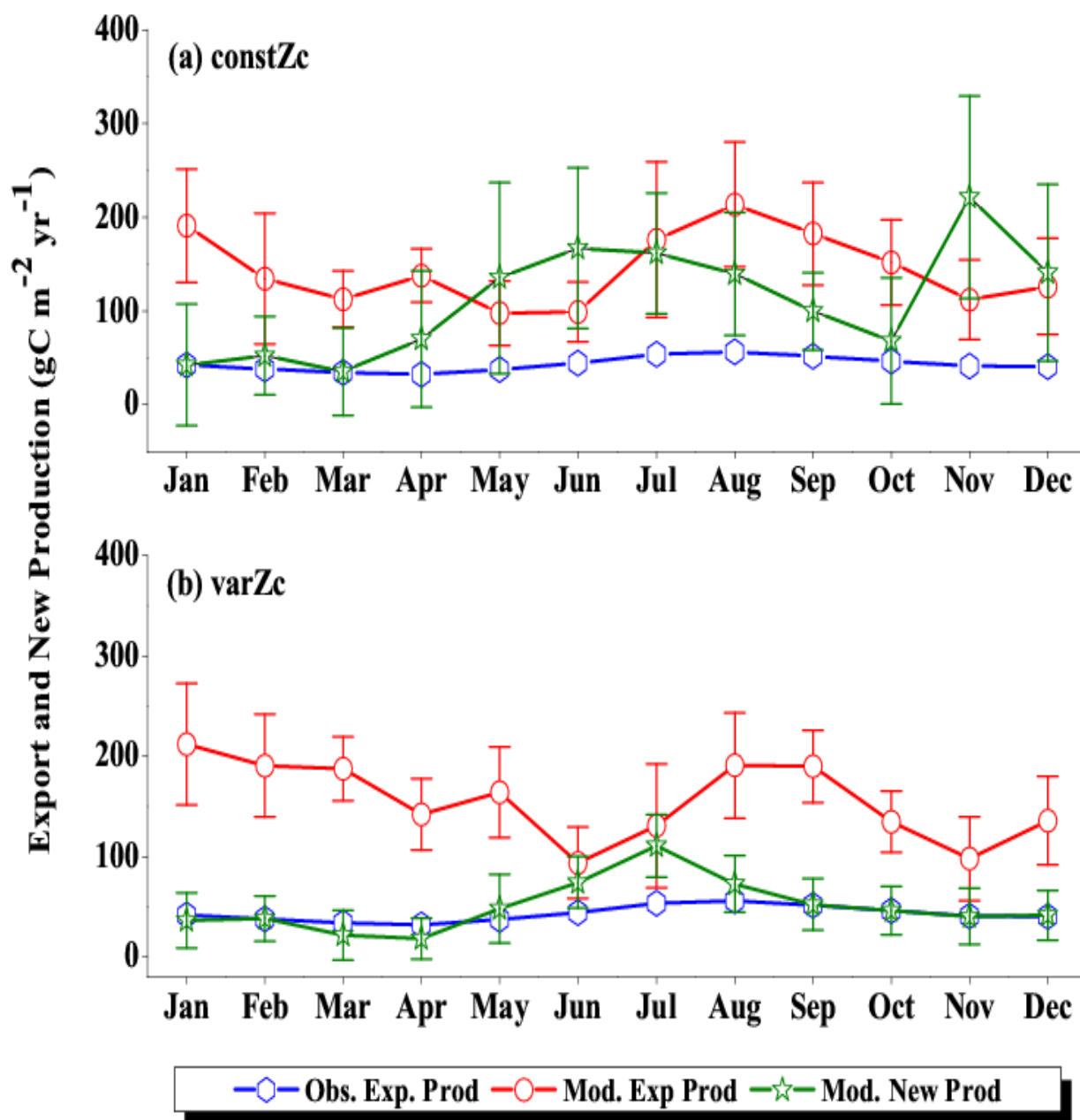


Figure 11: Same as Figure (7), but for SLD.

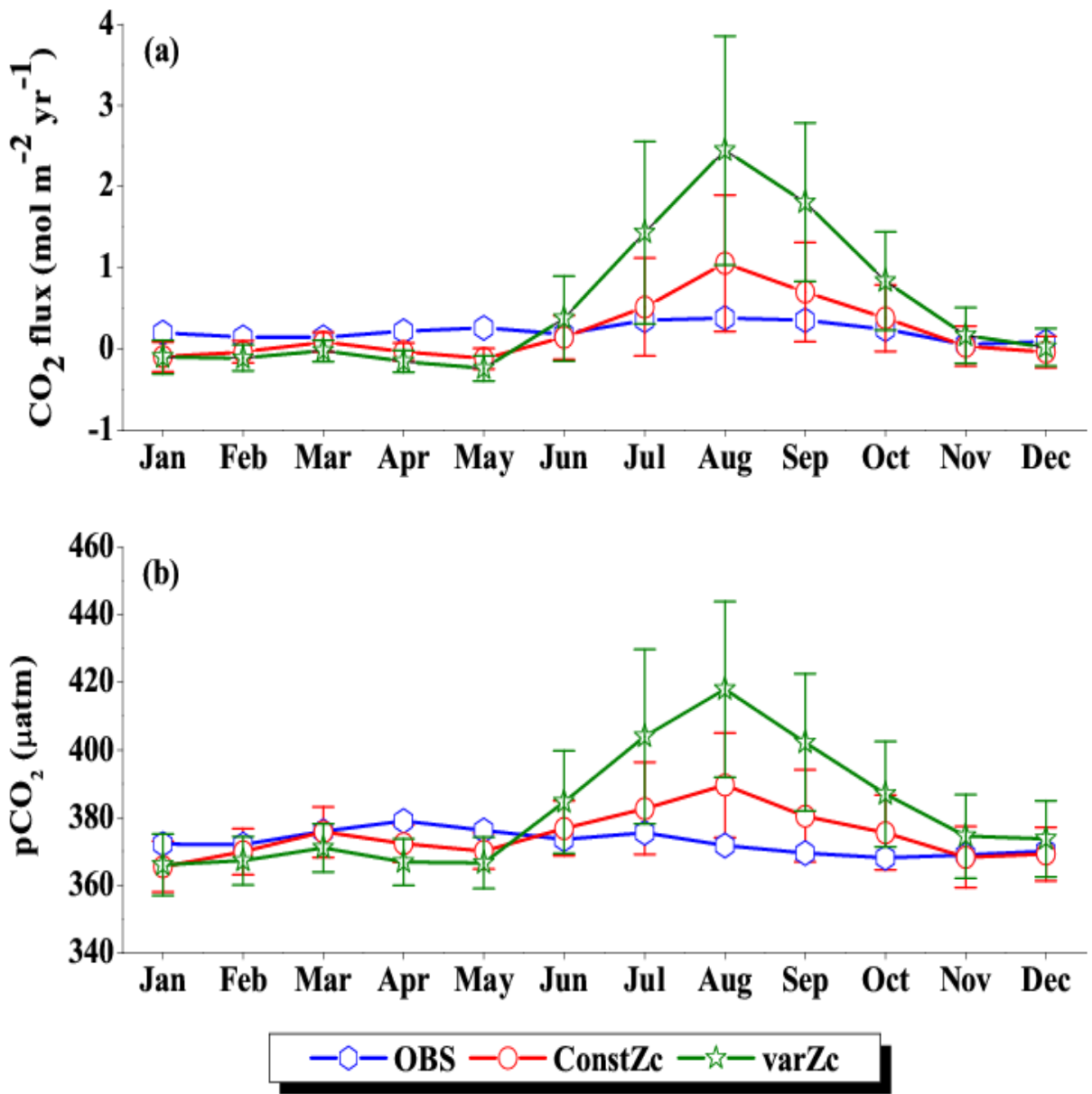


Figure 12: Same as Figure (6), but for SC.

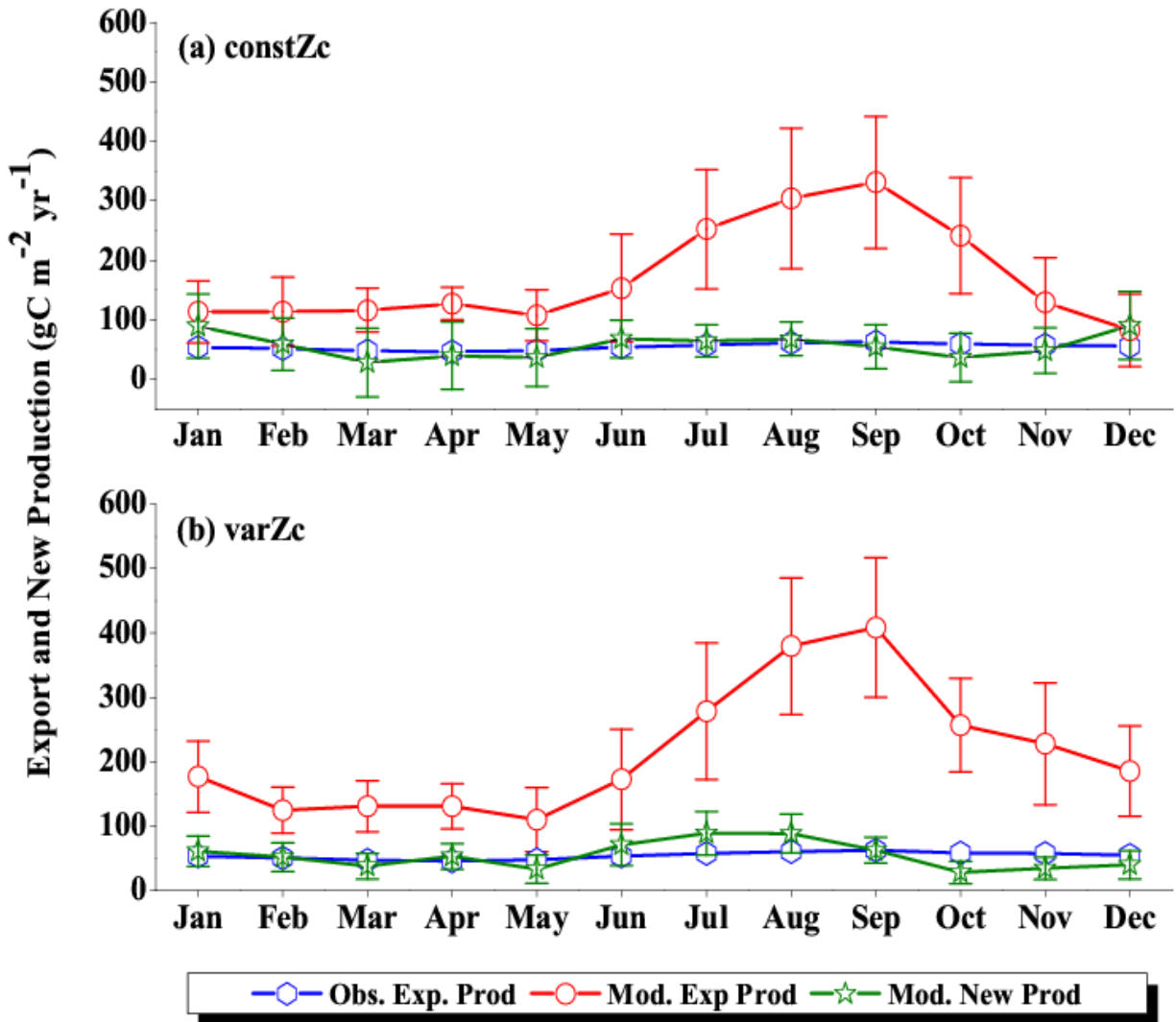


Figure 13: Same as Figure (7), but for SC.

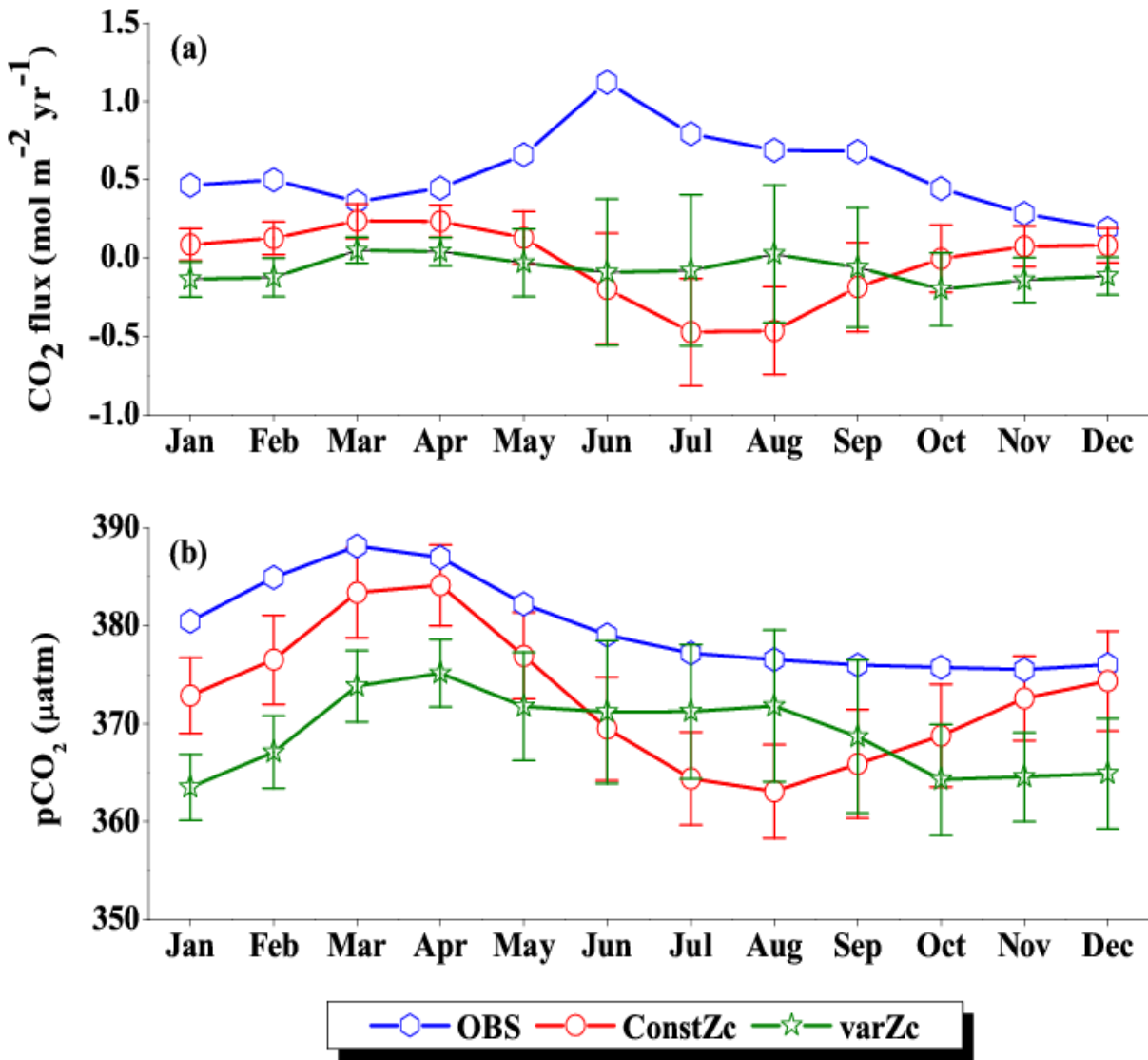


Figure 14: Same as Figure (6), but for SCTR.

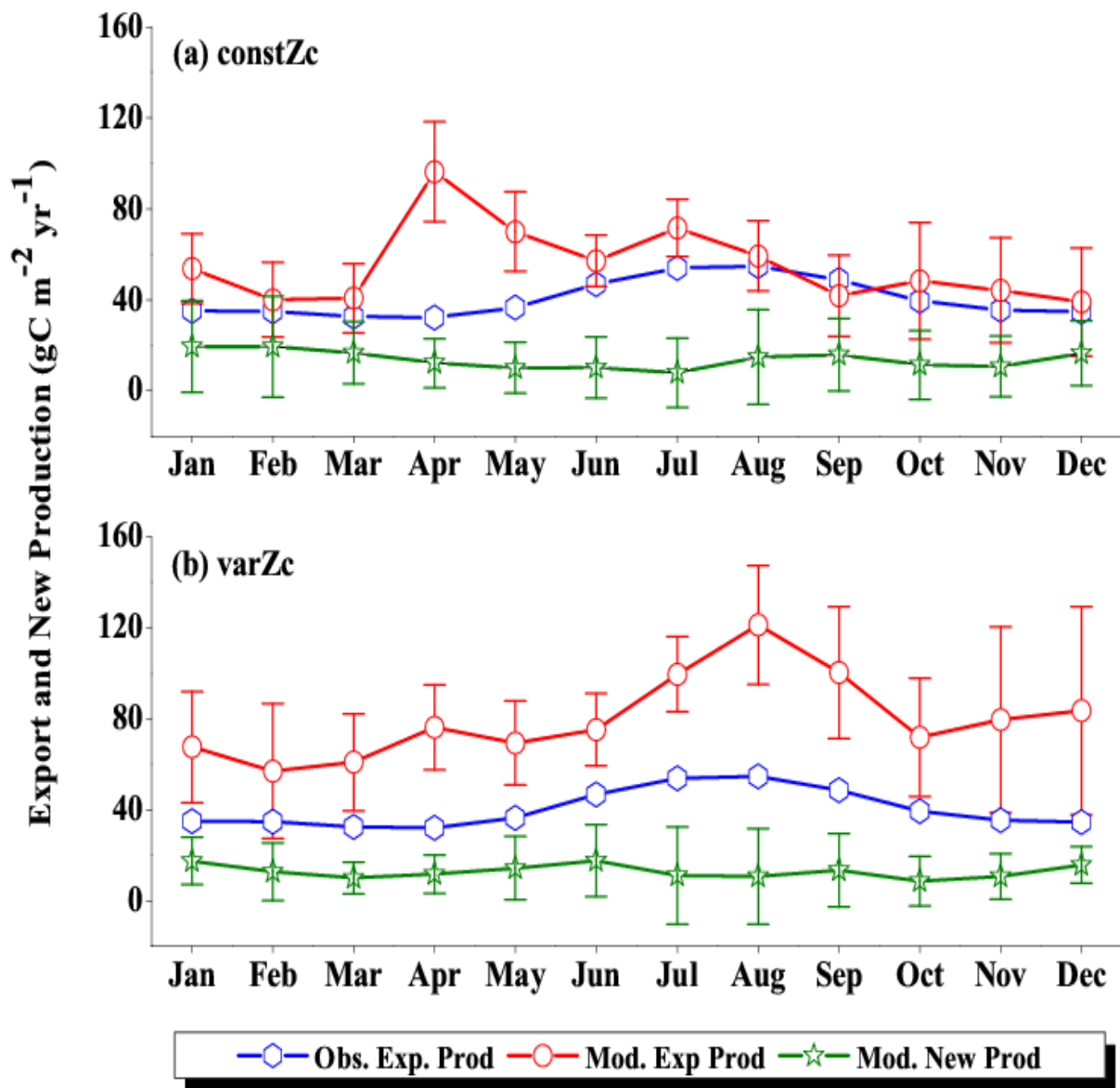


Figure 15: Same as Figure (7), but for SCTR.